Bore-Induced Local Scour around a Circular Structure

Alexandra Lavictoire

Thesis submitted to the

Faculty of Graduate and Postdoctoral Studies

In partial fulfillment for the requirements for the degree of

Master of Applied Science in Civil Engineering

Academic Advisors: Dr. Ioan Nistor and Dr. Colin D. Rennie

Department of Civil Engineering

University of Ottawa

2014

Abstract

Recent natural disasters, such as major tsunamis, have prompted researchers and practicing engineers to improve their understanding of the impacts of bore-like waves on structures and their foundations. The high velocity and the relatively short duration of hydraulic bores causes local scouring which is different from that generated by river flows and waves. The present study uses an experimental model to simulate the propagation of a hydraulic bore over a movable sediment bed placed around a circular pier-like structure. Measurements of water surface elevation, bore propagation velocity and scour distribution were taken. The linear relationship between reservoir depth and bore depth led to an increase in flow acceleration, and thus to an increase in flow velocity. Final scour bed elevations indicated that scour depth was highly dependent on the bore velocity. The scour depth ratios suggested in current design guidelines were significantly lower than those obtained in this study.

Acknowledgments

I must first acknowledge and sincerely thank my supervisor Dr. Nistor. I remember sitting in his fluid mechanics class in second year and realizing for the first time that water was my passion. It is thanks to his enthusiastic teaching and encouragements to pursue my studies in this field that I was able to succeed. Over the past few years, he kindly arranged amazing opportunities for me that not only improved my academic career, but also provided me with experiences that I will forever cherish. He has been a mentor and I would not have come this far without his support. I would also like to express my gratitude to my co-supervisor Dr. Rennie. This study would not have been complete without his knowledgeable input and active interest in continuously improving my research. He has been an invaluable and integral part of our small team.

I would like to recognize the generosity of all who helped me assemble and run my experimental model. Particularly Mark Lapointe, the hydraulics laboratory technician, who masterfully created my gate and helped me build my model exactly how I had envisioned it. I also extend my gratitude to the exchange, summer and graduate students who voluntarily shovelled gravel and coordinated the many tasks in each run. Your hard work is truly recognized and was key in the completion of my research.

I must also mention the support I received from my fellow graduate students who shared the offices with me in the hydraulics laboratory. Their always useful advice and good humour during stressful times made my masters experience even better.

Finally, I would like to thank my family. I will be forever grateful to my parents for having encouraged me in my academic endeavours. My accomplishments are a direct result of their love and support. To my soon to be husband, Rico, I express my deepest gratitude for his understanding and patience. His confidence in me over these past two years helped me focus on my research and attain my goals. To know that my family is proud of my work has made this stage of my life extremely rewarding and memorable.

Table of Contents

List of Tables

List of Figures

List of Symbols

b	pier width (m)
C	Chezy coefficient
c_b	shock wave celerity in the downstream direction (bore) (m/s)
c_u	shock wave celerity in the upstream direction (m/s)
D	sediment grain size (mm)
D_{50}	sediment median grain size (mm)
D_{gr}	dimensionless particle size parameter
d_s	scour depth (m)
F	Froude number
F_s	entrainment function
g	gravitational acceleration (m/s^2)
h_0	reservoir depth (m)
h_b	bore depth (m)
h_{max}	maximum bore depth (m)
h_u	upstream depth (m)
K_{yb}	depth-size factor
K_I	flow intensity factor
K_d	sediment size factor
K_s	pier shape factor
K_θ	pier alignment factor
K_G	channel geometry factor
K_t	time factor
ρ	water density (kg/m^3)
ρ_s	sediment density (kg/m^3)
R	hydraulic radius (m)
S	slope
t	time (s)
τ_0	shear stress (N/m^2)
τ_{cr}	critical shear stress (N/m^2)
u_b	depth averaged velocity of the bore (m/s)

u_{max} maximum propagation velocity (m/s)

υ kinematic viscosity of water

v_{cr} critical shear velocity (m/s)

x longitudinal position (m)

y flow depth (m)

z ground elevation of structure (m)

z_{max} maximum ground elevation attained by wave (m)

1. Introduction

1.1 Research Motivation

In recent years, a number of natural phenomena have impacted heavily populated regions of the world and caused in turn both unimaginable loss of life and extensive damage to infrastructure. Two such events were the 2004 Great Sumatra Andaman tsunami and the 2011 Tohoku tsunami. Both of these natural disasters mainly impacted coastal regions, but the waves were able to propagate much further inland and affect regions that were not expecting the tsunami and were therefore unprepared. Following these events, numerous teams of researchers flocked to the devastated regions to perform post-tsunami surveys of the damaged infrastructure. The results of these surveys varied widely, with evidence of structures damaged by a multitude of possible mechanisms. In many cases, structural failure of building components was caused by impact forces from the wave front or from debris in the flow, as well as from other tsunami-induced hydrodynamic forces. Surveys such as those conducted by Robertson and Francis (ASCE, 2010) of the Tohoku tsunami, observed the displacement of extremely heavy objects to large distances from the shore, further demonstrating the power of the tsunami waves. Figure 1 shows structures damaged by direct impact by debris or by wave impact on the lower levels.

Figure 1: Structures damaged by tsunami impact forces and debris (Left: Saatcioglu and Nistor (2006), Right: Nistor (2011))

In addition to structural damage caused by impact forces, a number of field surveys indicated the presence of local scour at building foundations. In surveys of India and Thailand following the Great Sumatra Andaman tsunami, researchers were able to document local scour occurrences at buildings located close to shore, but also at several kilometers inland. The pictures shown in Figure 2 provided an appreciation of the potential scour depths caused by the tsunami. Evidence of local scour was also observed and documented by a number of researchers in Japan following the Tohoku tsunami. Once again, the affected structures were located at varying proximities to the shoreline. The presence of local scour at structures located further inland indicated that the tsunami wave had extended its reach past the coastal zones and maintained a significant propagation velocity. This exact behavior was captured on live camera video recordings during the Tohoku tsunami. A number of news outlets provided live footage of the tsunami wave propagating in a perpendicular direction to the coast. A closer look at some of the video footage also revealed important characteristics of the tsunami wave. The wave front took the shape of a fully broken, turbulent roller as it propagated over the farmland in Figure 3. This distinct flow form closely resembles that of a hydraulic bore, a similar free flowing mass of water.

Figure 2: Tsunami-induced local scour at building foundations (Left: India (Yeh, 2004), Right: Japan (Nistor, 2012)

Figure 3: Tohoku tsunami bore-like propagation over Sendai farmland (Left: Right: NHK World News)

Due to factors such as the economic burden that resulted from the structural damage caused by the tsunamis, many researchers and engineers have been motivated to study the effects of tsunamis on structures. A number of physical or numerical studies aimed to recreate and measure these effects have been conducted in recent years. Given that the tsunami induced mechanisms causing damage are numerous and complex, the possible research paths in this field of study are plentiful. The experimental study at hand focused on the specific effect of tsunami induced local scour.

1.2 Objectives

The key objective of this study was to simulate the unique scouring process of a hydraulic bore and observe the formation of local scour at a circular structure. This research was conducted in the form of a physical experimental investigation. The use of a flume, a structure model and different types of sediment allowed for a custom set up at a reasonably large scale. The use of a numerical model may have enabled more test runs to be performed; however the scouring process was first attempted in a physical environment. This investigation was also intended to complement the research conducted by Al-Faesly et al. (2012) on tsunami-induced hydrodynamic loading on structures.

The main experimental goals of this study were to generate a laboratory hydraulic bore and observe the scouring process it induced around a circular structure. Further objectives included the measurement and analysis of bore characteristics, such as bore depth, bore front velocity and the sustained flow velocity. The quantification of these results ensured that true hydraulic bores were being generated. Objectives related to the local scour included analysis of the scouring process and final scour depths. Finally, the relationship between the local scour depths and the bore characteristics was derived.

1.3 Novelty

Many aspects of this study are novel to this field of research. Although studies on the impacts of tsunami induced forces on structures are numerous, there have been few studies focusing on the scour caused by tsunami waves. The examination of local scour at a structure caused by a tsunami-like wave has thus far only been investigated in two studies (Tonkin et al., 2003; Nakamura et al., 2008). The tsunami waves in these studies were simulated using solitary and long waves, unlike the hydraulic bore simulation used in the present study. Furthermore, the current study focuses on inland structures located on a dry horizontal bed, rather than structures located close to shore on sloped beaches.

The dearth of previous research on tsunami induced scour has resulted in a lack of documentation of tsunami induced scour in structural design guidelines across not only North America but also for the rest of the international scientific community Although the potential for this type of scour is present, its quantification and estimation has not yet been studied in depth. Therefore, design guidelines currently provide only minimal information and mitigation suggestions for tsunami induced scour at structure foundations. It is intended that this study will provide a better understanding into this unique scouring process, and will contribute to the development of methods to estimate local scour for future application in design guidelines.

2. Literature Review

2.1 Definition of Hydraulic Jumps, Bores and Jets

Very turbulent, supercritical flows may be categorized as hydraulic jumps, turbulent bores and jets. Although all three of these terms describe highly aerated flows with high Froude numbers, they do possess certain differing characteristics.

Hydraulic jumps occur at the point of transition between a supercritical and a subcritical flow. It is a region of rapidly varied flow, which results in the development of turbulence, air entrainment and surface waves and spray. Due to its extremely turbulent nature, a hydraulic jump is also the location of extensive energy dissipation. They are often used as energy dissipaters at the end of spillways or over weirs. Hydraulic jumps are usually stationary, resembling a partially submerged roller or a cluster of vortices.

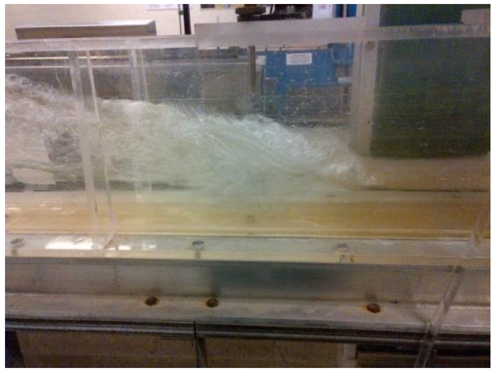

Figure 4: Hydraulic Jump in a Laboratory

A hydraulic bore is defined as a fully broken wave, propagating over land or water. Some examples of hydraulic bores occurring in nature are tidal bores, tsunami waves and flood waves, with images pictured below. The source of the bore can be highly variable, such as the rapidly advancing tidal wave fronts or dam/dike failures. However, the resulting bores have similar characteristics. Hydraulic bores can reach very high velocities and often maintain a constant significant depth during their propagation. Due to the conditions in which bores form, they have a relatively short duration. They resemble a hydraulic jump in that the surge front is very turbulent. However, in this case, the wave front moves. Surge fronts will advance when there is an increase in depth and will retreat when there is a decrease in depth, thus becoming either positive or negative surges respectively.

Figure 5: Hydraulic Bore Traveling up the Petitcodiac River, New Brunswick

The formation and characteristics of hydraulic jumps and bores have been the subject of many studies. Certain types of jumps and bores have been observed to coincide to specific Froude numbers and to certain downstream and upstream conditions. In their experiments on hydraulic surges, Koch and Chanson (2009) observed an array of different surges, such as undular surges and fully broken surge waves. He also determined that the degree of wave breaking in a surge is proportionate with the Froude number of the upstream flow.

Figure 6: Undular Bore and Fully Developed Bore (Koch & Chanson, 2009)

Hydraulic jets are also defined as a turbulent flow, yet unlike jumps and bores, they do not occur due to a change in flow conditions. Jets may be formed in various ways. Free falling water, such as a water fall or from a spillway, causes a turbulent flow of water within the receiving water body. Some jets are also caused by variations in pressure, such as at the bottom of a sluice gate that is opened very little. Jets often have a distinct direction of flow and may be more local.

Figure 7: Hydraulic Jet caused by a Horseshoe Waterfall (Pasternack, Ellis, & Marr, 2007)

2.1 Hydraulic Bores in Laboratory

The equations governing the movement and shape of hydraulic bores are related to the dam break equations and can be derived from experimental work. In his book on water waves, J.J. Stoker developed equations for hydraulic bores based on his shallow water theory (Stoker, 1957). Stoker explored the theory behind waves occurring in shallow water depths, and using the method of characteristics, was able to develop a system of differential equations closely related to those of the motion of compressible gasses. He was then able to explore specific cases such as shock waves and provided simplified equations for more practical uses.

For the purposes of this research, Stoker's solutions for the breaking of a dam best simulate the propagation of a tsunami wave. He analyzed a fictitious scenario to mimic the sudden removal of a dam, releasing a volume of water contained in a reservoir of a predetermined height and of an infinite length. By assuming an upstream reservoir height, the downstream bore conditions can be analytically determined by dividing the downstream section into different parts with distinct flow conditions. As shown in Figure 8, the zones distinguish between the upstream reservoir (u), the bore like wave (b), a flow of constant state (s) and the downstream wet bed (w). Stoker also treats two different cases. That of a downstream section initially free of water and the case where the downstream section contains water of a constant depth.

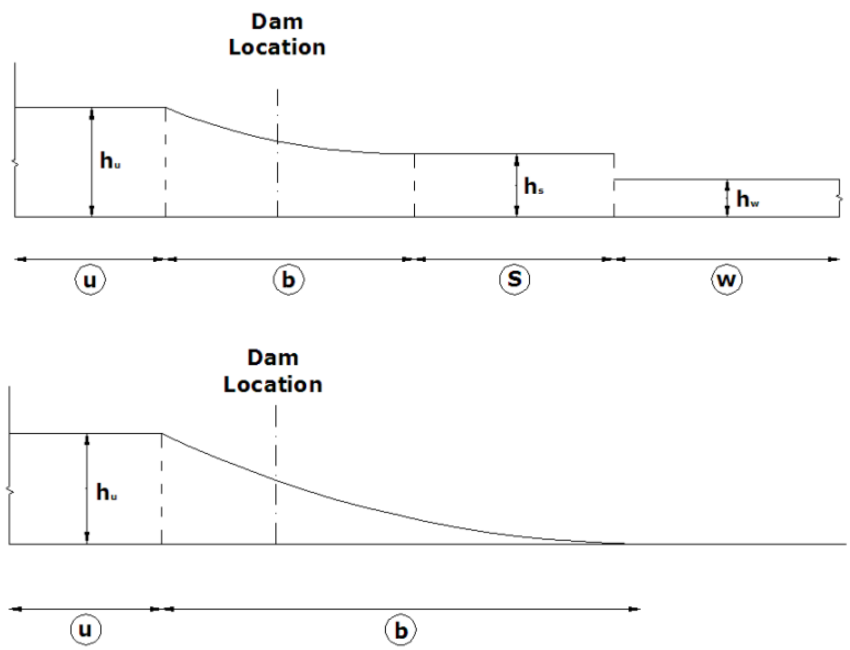

Figure 8: Schematization of the Dam Break Wave Propagation

The zones pictured here include three permanent zones. Zones (w) and (u) being those of undisturbed or quiet water. Zone (s) is also at constant state although the water in it is not at rest. And finally zone (b) is represented by a simple wave that connects zones (u) and (s). In the case of the dry downstream section, zones (s) and (w) do not exist and zone (b) directly connects the reservoir of zone (u) to the dry channel floor.

Stoker developed the expressions for the shock wave conditions between the different zones in order to create equations for the water depth and velocity of the advancing bore. He was able to derive the following three equations describing the bore:

$$h_b = \frac{c_b^2}{g} \tag{1}$$

$$c_b^2 = \frac{1}{9}\left(2c_u - \frac{x}{t}\right)^2 \tag{2}$$

$$u_b = \frac{2}{3}\left(c_u + \frac{x}{t}\right) \tag{3}$$

All terms in these equations are defined in the list of symbols. For the purposes of this study, a dry, frictionless, downstream bed is assumed, and thus these equations only take into account zones (u) and (b) are of interest. Other assumptions made for these equations are that viscosity and turbulence are neglected, as well as that the hydrostatic pressure and fluid velocity are taken as uniform over the depth.

Upon examination of equations 4 to 6, it can be observed that the water surface profile in zone (b) is a parabolic curve. There is also a discontinuity of the slope of this parabola at its junction with zone (u). An interesting phenomenon also occurs at the location x=0. At this point, which corresponds to the initial dam location, both c and u are independent of time. The water surface elevation and depth normalized velocity are held constant at $h=4/9h_u$ and $u=2/3c_u$ for all time t at this point.

Experimentally, bores are physically simulated in small or large flumes by controlling flows with gates and submerged structures. In this way, the method of simulation closely follows theory, as the upstream and downstream flow conditions are set in such a way that a hydraulic jump or bore is created. Some examples of experimentally simulated hydraulic jumps include Adduce et al. (2006) and Farhoudi et al. (1985) studies, in which a hydraulic jump is created when water flows over a spillway like structure.

The experimental simulation of a hydraulic bore over an initially dry bed has been the topic of research for many as it is a natural phenomenon that is more difficult to recreate in laboratory. In some instances, hydraulic bores are recreated as wave runup caused by a solitary or long wave (Tonkin et al. 2003 and Nakamura et al. 2008). Although this method produces the desired bore effect, the duration and height of the bore are small, and the bore does not propagate with the same force as a tsunami or flood wave. Therefore, an alternate method of simulating hydraulic bores over a dry bed by a dam break method has become common. This method consists of suddenly releasing an enclosed volume of water, in order to create a free surface through which the hydraulic bore may form and propagate. Al-Faesly, et al. (2012) and Arnason (2005) retained a reservoir of water behind a swinging gate and suddenly allowed the gate to swing open in order to create a hydraulic bore. Similarly, Ramsden (1993) also held a reservoir of water behind a gate. As opposed to letting the gate swing, a piston was used to quickly lift the gate in a vertical motion. Chanson, et al. (2003) also explored such methods by creating a hydraulic bore from the sudden release of water from a tank located above a flume. The jet generated from the impact of the water on the flume bottom displaced itself like a hydraulic bore.

Figure 9: Left: Sudden Gate Opening (Al-Faesly et al., 2012)
Right: Vertical Drop of Water Volume (Chanson et al., 2003)

There are a number of factors that affect the hydraulic bore formation and propagation. For the purposes of this literature review, the two main factors that come into play are the time of removal of the gate and the condition of the downstream bed. The theory behind the dam-break problem suggests that the gate representing the dam is removed instantaneously in order to achieve a free displacement of the impounded water. In reality, the instantaneous removal of a gate is impossible to achieve. The gate must therefore be removed in a time short enough that the free surface of the impounded water is not restrained and that it may propagate freely. Lauber, et al. (1997) demonstrated through experiments in a horizontal channel with a sliding gate, that an ideal dam-break condition is achieved if the nondimensional removal period $(g/h_0)^{1/2}t < 2^{1/2}$, where h_0 is the reservoir depth and t is the removal time.

As was presented in the section on Stoker's dam break wave equations, the dam-break problem can be examined with a downstream section being either a dry bed or a wet bed. Theoretically, the bore formation and propagation is different for the two cases. This is especially interesting experimentally, as a perfectly dry bed is very difficult to achieve. Stansby, et al. (1998) performed a series of tests on dry and wet downstream beds for the sudden dam-break problem and their results show remarkable differences between the various downstream conditions. Their experiments were carried out in a flume with a square cross-section of 0.4 m x 0.4 m and a length of 15.24 m. The bed of the flume was horizontal and its walls made of clear

Perspex in order to allow for video recordings of the advancing bore. The gate used in this setup was a sliding plate that was suddenly lifted by dropping a weight attached to the gate through a system of ropes and pulleys. The gate was located at 9.72 m from one end of the flume and was completely withdrawn from the flume in approximately 0.1 seconds.

Experiments were carried out for reservoir heights, h_0, of 0.1 m and 0.36 m, and for downstream water depths of 0, $0.1h_0$ and $0.45h_0$. Thus, the downstream conditions were either dry, a very thin layer of water, or a more substantial downstream water depth. For each test, the flow was illuminated by a laser light sheet and simultaneously filmed by a video camera in order to capture snapshots of the bore formation and propagation. Perspex® powder was also added to the surface of the reservoir water in order to provide additional illumination of the water surface in the laser light. The following images show the results for the three different downstream conditions, with flow propagating from left to right.

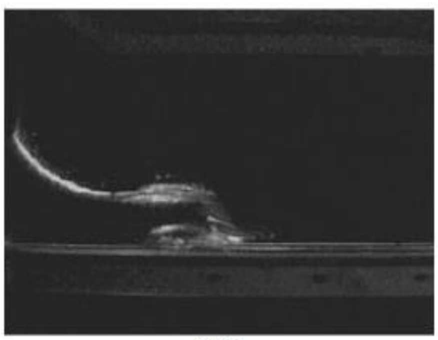

0.24 s

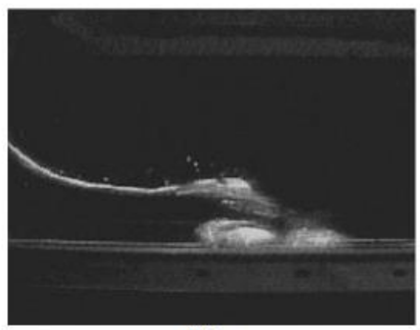

0.32 s

$t = 0.20$ s

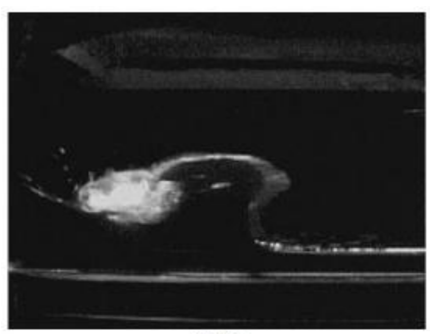

0.36 s

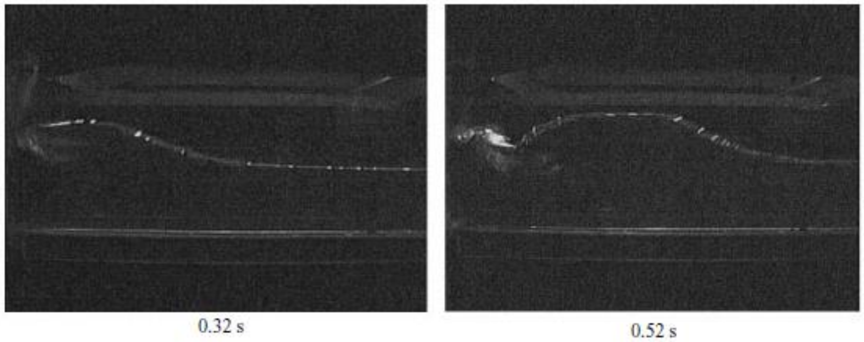

Figure 10: First two frames: Dry downstream bed, Second two frames: 0.1h0 downstream bed, Third two frames: 0.45h0 downstream bed (Stansby, Chegini, & Barnes, 1998)

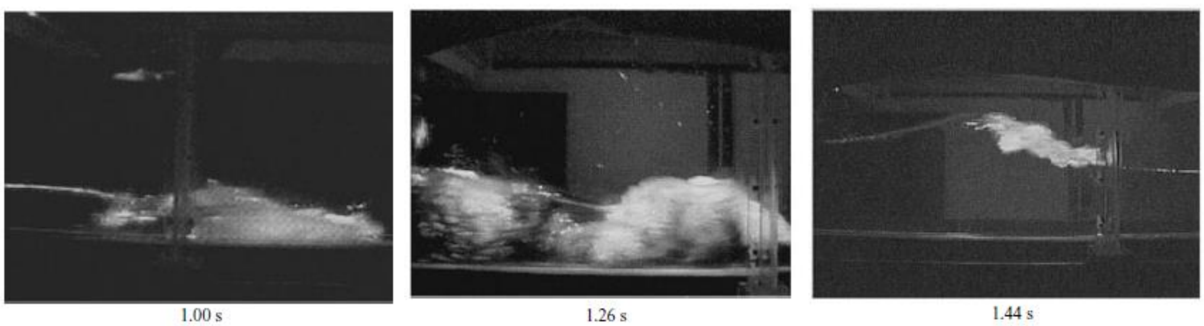

Figure 11: Final frame of dry downstream bed, 0.1h0 downstream bed and 0.45h0 downstream bed (Stansby, Chegini, & Barnes, 1998)

The observations collected by Stansby et al. (1998) show that the bore formation differs greatly depending on the downstream condition, yet the flow eventually reaches a constant bore shape and a similar propagation is observed. The dry bed condition has the effect of producing an almost instantaneous bore. The bore front has an initially greater height and variable shape. For a very small downstream water depth ($0.1h_0$), a distinct mushroom shape forms vertically over the front of the bore. The elevated water then curls forward and causes a splashing wave which propagates forward to eventually become a steadier bore. Finally, in the case of a larger downstream water depth ($0.45h_0$), a bore formation is not present. Instead, there is the formation of a wave which breaks much like a spilling breaker.

This study shows that although the initial behavior of the water jet may vary for the downstream condition, the further propagation of the water stabilizes to that of a well-defined hydraulic bore. In the case of tsunami or flood waves, one could therefore presume that although the initial formation of the wave as it hits either land or other water bodies varies, the inland propagation of the wave can be compared to that of an advancing hydraulic bore.

2.3 Types of Scour and Erosion

The transport of sediments induced by the flow of water is a complex phenomenon. Whether it occurs in rivers, man-made channels, lakes, estuaries or oceans, the aggradation and degradation of the sediment beds is an ongoing process. In general, this sediment transport mechanism can be categorized into two broad classes, scour and erosion (Chanson, 2004). Scour describes any sediment movement that occurs in a vertical direction, and is always related to a decrease in sediment bed elevation. Erosion describes the action of sediment removal from the bed. With erosion, accretion also occurs in areas of the bed where the eroded sediment is then later deposited. Often, both types of sediment transport may occur simultaneously and thus the pattern of the sediment movement is very complex and varies not only through space, but also through time. The following section will provide further explanations of both scour and erosion in riverine settings, as well as give examples of each.

Scour itself can be further divided into global or general scour and local scour (Chanson, 2004). Global scour is defined as a vertical degradation of the sediment bed in general. It may occur in a uniform or non-uniform pattern across the width of the given flow. This type of scour is often observed when there is a sudden contraction of the flow or a bend in the flow. Sudden large flows, such as flood waves, may also cause global scour.

Local scour on the other hand is characterized by a vertical change in bed elevation at a specific area of the bed, most often near or around a structure. The sudden obstruction of the flow due to a structure causes an acceleration of the flow and vortices to form around it. The forces created by these vortices cause the removal and deposition of the sediment around the structure (Melville, 1975). Local scour develops in a specific pattern depending on the flow characteristics and the specific shape of the structure.

Figure 12: Scour Hole around a Bridge Pier on the Platte River, Nebraska (http://thestagnationpoint.blogspot.ca/)

Erosion, as previously stated, consists of the lateral displacement of the sediment bed. For example, in rivers with slower flows, the flow direction is prone to change, thus causing the sediment to follow and gradually move the main bed of the river. Erosion is also present at the outlet of large rivers into the ocean, where sediment being transported by the river is deposited in the form of an alluvial fan.

2.4 Scour and Erosion Studies and Equations

The study of scour and erosion has its difficulties especially because of the ever evolving mechanism of scour and of the multitude of variables involved in the development of scour. Not only do the characteristics of the sediment come into play, but the complexity of the flow of water make it difficult to assess exactly how the scour is occurring at different points in time.

In their study on scour around circular bridge piers, Jain et al. (1979) presented a comprehensive overview of scour equations. In general, all scour equations stem from the same basic equation relating the scour depth to four important variables. This equation can be written as follows:

$$\frac{d_s}{b} = A\left(\frac{y}{b}\right)^m (F)^n + B\left(\frac{D}{y}\right)^p \left(\frac{y}{b}\right)^r \tag{4}$$

In which, d_s is the scour depth, b is the width of the pier, D is the sediment grain size, y is the flow depth and F is the Froude number. All other variables are constants or exponents dependant on the specific equations. Therefore, it is possible to conclude that scour depth is a function of pier size, flow depth, flow velocity and sediment grain size.

From the multitude of scour equations reviewed by Jain, et al. (1979), a few key points have emerged. Although most scour equations are based on the equation outlined above, the estimates of scour depth differ widely from one equation to the next, and this especially in supercritical flows. This may be due to the fact that most often, scour equations are derived from experiments carried out on a specific range of flow conditions. Thus, extrapolation of the equations to other flows diminishes their validity and leads to mixed results from different equations. Jain, et al. (1979) also indicated that in most scour experiments, scour depth measurements are taken once the flow has been stopped. This allows for deposition to occur and therefore the final scour depth which is measured is not the actual maximum scour depth. Although adjustments may be made to equations for this effect, in cases where flow velocities are high, the effect is more pronounced and harder to control.

A more recent equation developed to estimate local scour depth was developed by Melville and Coleman (2000) in their book *Bridge Scour*. Their equation relates the local scour depth at a pier or abutment to a combination of factors each affecting scour in a different way. The equation for pier scour is as follows:

$$d_s = K_{yb} K_l K_d K_s K_\theta K_G K_t \tag{5}$$

The factors in this equation are for depth-size (K_{yb}), flow intensity (K_l), sediment size (K_d), pier shape (K_s), pier alignment (K_θ), channel geometry (K_G) and time (K_t). Many of these factors are similar to those previously proposed by Jain, et al. (1979). For the Melville and Coleman (2000) equation, further definition of each factor is provided in the form of secondary equations or constants based on the situational variables of the pier at hand.

The novelty of the Melville and Coleman (2000) equation lies in the addition of a time factor to the scour depth equation. This time factor relates the scour depth at the given time to the equilibrium scour depth which occurs at the equilibrium time. For the case of live-bed scour, the equilibrium scour depth is usually attained quickly and so this factor is set to unity.

However, in the case of clear-bed conditions, the time to reach equilibrium scour depths could be important and so an approximation of the degree of scour at the given time is represented by this time factor. This way, the local scour depth is less likely to be greatly over estimated.

2.5 Mechanism of Local Scour around Structures

The subject of local scour around pier-like structures has been the subject of much research and its distinct mechanisms has been described by many authors. Jain, et al. (1979) provided a description of the process, based on the common observations of many researchers and as described by Melville (1975), which will be the basis of the following explanation.

Local scour around structures is initiated by the obstruction of the flow by the structure itself. This obstruction forces the flow to propagate at higher velocities in all directions around the structure. The portion of the flow that is diverted downwards forms an initially small horseshoe vortex directly in front of the structure. The vortex slowly causes the sediment to dislodge itself from the bed, and a scour hole forms. As the scour hole grows, additional fluid enters the horseshoe vortex and causes it to expand in size and strengthen its downflow. The circulation motion of the vortex continually increases, due to the expansion of the scour hole. However, as the scour hole progresses upstream from the leading surface of the structure, the portion of the flow being supplied to the downflow of the vortex decreases and thus the scour hole increases at a decreasing rate. Equilibrium around the structure is attained when the downward flow of the vortex is no longer strong enough to displace the sediment at the bottom of the scour hole.

The mechanism of local scour around structures also includes the deposition process of the sediment that is gradually removed from the scour hole. Deposition occurs on the sides and behind the structure in the form of dunes or banks. The deposited sediment accumulates at a specific distance away from the structure and in a specific shape depending on the flow conditions and on the shape of the structure. In some cases, deposition may also occur within the scour hole, creating irregular bed elevation in front of the structure.

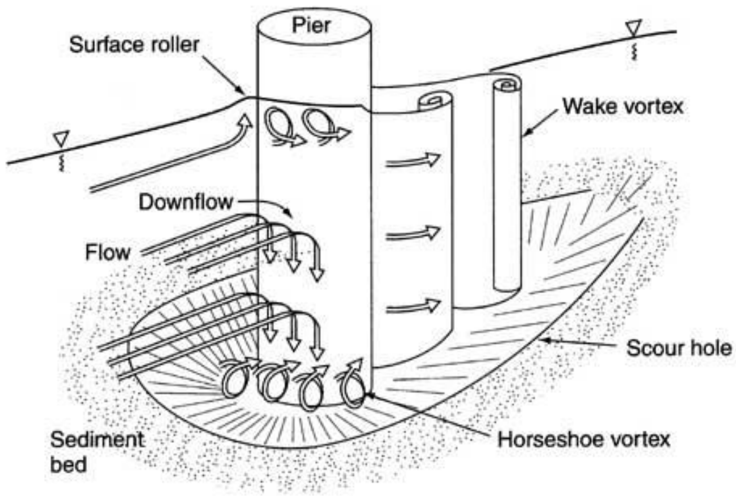

Figure 13: Schematic Representation of Vortices Creating Local Scour (Hamill, 1999)

2.6 Local Scour around Structures in Supercritical Flows

This section will focus on research conducted on local scour around pier-like structures for two cases of supercritical flow, but not specifically hydraulic bores. The first study, by Jain, et al. (1979) comprises of physical experiments on local scour around circular bridge piers at relatively high Froude numbers. The second topic to be explored in this section is the local scour around piers caused by jets. Both cases evaluate scour around structures in very turbulent flows.

The experiments of Jain, et al. (1979) were performed in a tilting sediment flume, with two circular piers of different diameters and with varying sediment grain sizes and flow velocities. The sand bed depth and flow depth were maintained for all the tests. The main objective of this study was to observe the mechanisms of local scour at the pier, such as in clear water scour experiments, and also the changes in scour at the pier caused by the sediment transport regime in the channel. At high Froude numbers, a sediment transport regime is inevitable, and thus the scour at the piers is not only defined by the changes in flow due to the pier, but also by the changes in flow due to the bed forms shaped by the general sediment transport. This is described as live-bed conditions.

The tests were carried out with two piers in sequence and at flow rates with Froude numbers ranging from 0.5 to 1.5. Each run had a duration long enough for multiple bed formations to develop and migrate past each pier, as well as for the local scour to attain its equilibrium. The results indicated that the maximum local scour depth was always observed at the downstream side of the piers. The contribution of the scour caused by bed forms increasingly affected the local scour depths at the piers as the velocity increased. Jain, et al. (1979) developed an equation for scour based on a regression analysis of their experimental data.

They also discovered a phenomenon in increasing and decreasing scour depth for a specific range of Froude numbers. As shown in the two graphs below, their results showed that for instances where the difference between the Froude number of the flow (F) and the critical Froude number (F_c), taken as the Froude number for the critical velocity causing sediment motion, was lower than 0.15, the scour depth decreased as the velocity of the flow increased. Past this threshold value, the scour depth increased as the velocity of the flow increased, as would generally be expected. This decrease in scour depth was attributed to the effects of the sediment transport regime for those specific flow conditions. In the cases where ($F-F_{c)}$ < 0.15, the rate at which the vortex was able to remove the sand from the scour hole was smaller than the rate at which the incoming flow transported sediment into the scour hole. This observation was only possible for tests performed under the live-bed sediment transport regime.

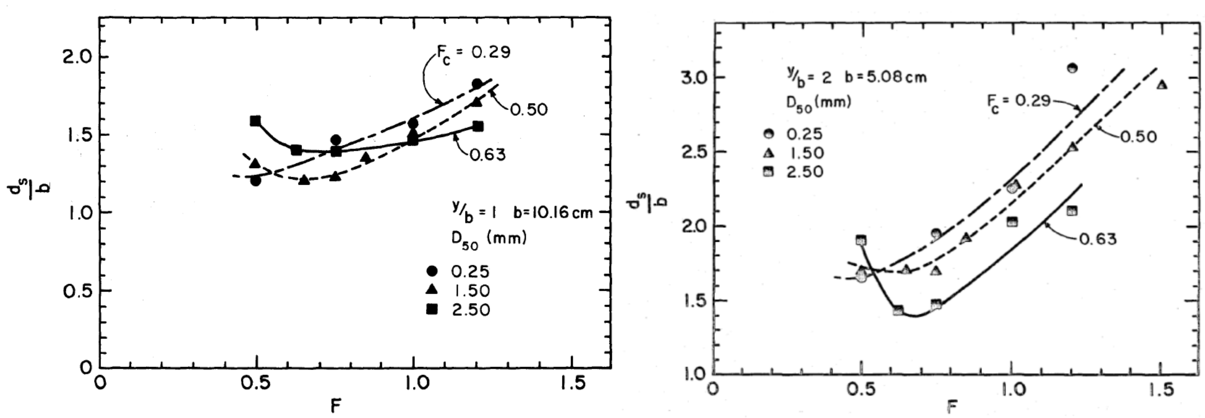

Figure 14: Relative Scour Depth around Circular Piers for Flows with High Froude Numbers (Jain & Fischer, 1979)

Other experimental investigations dealing with local scour around piers due to very turbulent flows are studies on the impacts of the jets caused by boat propellers on the underwater structures of harbours. Researchers such as Yuksel, et al. (2005) and Chin, et al. (1996) have shed light on the scouring mechanism of these complex flows. Unlike most scour investigations which have dealt with steady current flow around a circular pier, the complex jet flow caused by boat propellers or other turbulent flows has been less researched.

The configuration of the experimental tests performed by Chin et al. (1996) consisted of a water jet created by a nozzle located just above a horizontal sediment bed, with one or two circular piers located at specific distances downstream and along the same axis as the nozzle. The water level covering the sand bed and the piers was fixed and immobile. Chin, et al. (1996) observed similar scour results as those of clear water bridge pier scour. In the case of the jet scour, the scouring mechanism was generated by the high velocity of the jet flow. The horseshoe vortex formed on the upstream side of the pier and caused a scour hole to form, with the displaced sediment settling at the back of the pier. The temporal development of the local scour was surprisingly fast. Within the first hour of scouring, the scour depth had reached over 80% of its maximum equilibrium scour depth and the portion of the scour hole between the jet outflow and the maximum scour depth was almost fully developed.

Yuksel, et al. (2005) performed very similar experiments on jet induced local pier scour. The main difference is that they also tested for jet locations at vertical offsets from the sediment bed level. Their results were very similar to those of Chin, et al. (1996), as they also observed a distinct scour hole formation, and a zone of deposition behind the pier. The vertical offset of the jet caused the depth of the scour holes to decrease, as the height of the jet from the sediment bed increased.

2.7 Sediment Motion beneath Bores

Current studies found in literature pertaining to scour caused by hydraulic bores are mostly related to the effects of tidal bores on the river sediment beneath them or the effects of tsunami waves on sediment, brought on by the 2004 Great Sumatra Andaman Tsunami. The first subject matter, sediment transport induced by tidal bores, has been extensively studied in the field and experimentally by Hubert Chanson and many co-authors. In 2010, Chanson, et al. (2010) conducted a field study of the tidal bore occurring on the Garonne River in France. They used Acoustic Doppler velocimetry to measure this undular bore's velocities, turbulent characteristics and suspended sediment concentration. Their results showed that the bore caused a complete reversal of the flow direction in the river and that it travelled upstream at a constant depth and velocity, as shown in Figure 15. The suspended sediment concentrations were determined by calibrating the ADV backscatter amplitude. The results indicated that the bore caused the sediment transport to switch from a downstream direction to the upstream direction. In addition, although the bore passage cause sediment to be entrained upstream, the upward advection of the suspended sediments towards the free surface was delayed.

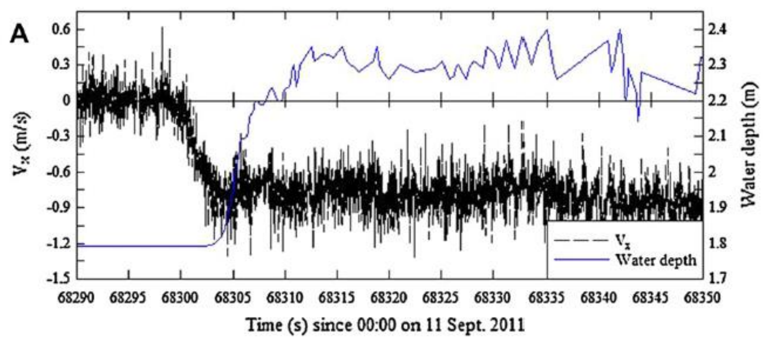

Figure 15: Tidal Bore Depth and Streamwise Velocity (Chanson et al., 2010)

A similar type of research was later conducted by Chanson and Khezri, in which the inception of sediment motion beneath a tidal bore was simulated and evaluated in a laboratory. This study focused on determining what forces and pressures played the most important roles in dislodging and transporting gravel particles located beneath undular and breaking bores. Their results first provided the distinction between undular and breaking bores. With undular bores occurring at Froude numbers between 1 and 1.3, and fully broken bores occurring at Froude number above 1.3 to 1.4. As for the sediment motion induced by these bores, Chanson and Khezri did not observe any sediment motion beneath the undular bores. The sediment motion was mainly induced by the passing of the roller toe of the fully broken bores. The gravel particles were initially de-stabilized by the longitudinal pressure gradient and further transported upstream by the drag force. The average upstream sediment transport velocity was 14% that of the bore celerity, with maximum sediment velocity values of 69% of the bore celerity.

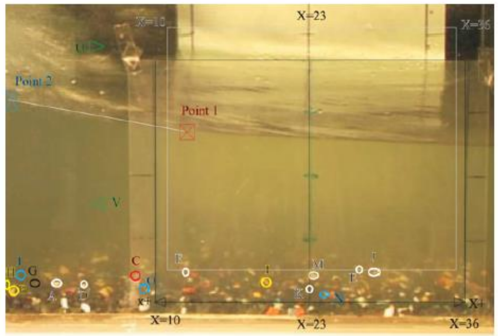

Figure 16: Gravel Particles in Motion beneath a Bore (Chanson and Khezri, 2012)

The second most prevalent research area focuses on physical and numerical experiments of sediment transport and scour caused by tsunami like waves. Yoshii, et al. (2010) physically and numerically simulated the pick-up rate of suspended sand within a harbour caused by a tsunami wave. Their results showed scour at the heads of the breakwaters defining the entrance of the harbour and slight aggradation in the central zone of the inner harbour. Similarly, Moronkeji (2007) created a physical experiment to assess the scour and deposition of sand caused by a tsunami wave over a sloped bed. The changes in the bed profiles were compared to measurements of pore pressure within the sand in order to find a correlation between scour caused by uplift within the soil skeleton.

Experiments related to scour around structures caused by tsunamis are limited to very few studies. Two studies that are the most related to the research at hand will be reviewed in detail in this section. The first, by Tonkin et al. (2003), examined scour around a cylindrical structure located on a sloped sandy beach, whereas the other study by Nakamura, et al. (2008), focused on scour around a square structure located on a horizontal sand bed. Both studies underlined the important difference between tsunami scour and pier or wave scour, in that tsunami scour occurs during transient flows. These flows of short duration, yet high turbulence, are unique in that during the flow period, pore pressure gradients may form within the soil substrate, thus enabling local scour. Tonkin, et al. (2003) paid special attention to this phenomenon in their study, as will be discussed below.

Tonkin, et al. (2003) used a pier like cylindrical structure made of Plexiglas for their physical scour experiments. The structure had a diameter of 50 cm and was located near the crest of a 1:20 sloped sand beach, with a median grain size of 0.35 mm. For certain tests, a gravel collar (D_{50}=3.6mm) surrounded the base of the cylinder. The tsunami waves were simulated by generating solitary waves using a piston type wave maker at a location offshore from the sand slope. Based on runup heights, the scale of the waves was approximately 1:10 of a realistic tsunami wave.

Measurements were taken using capacitance type wave gauges, pressure transducers, electromagnetic flow meters and miniature CCD cameras. The pressure transducers were placed in the sand below the initial level of the bed and the cameras were located inside the cylinder. The parameters varied in the different test runs were the still water depth, the incident wave height, the embedded depth of the cylinder and the presence or not of the gravel collar.

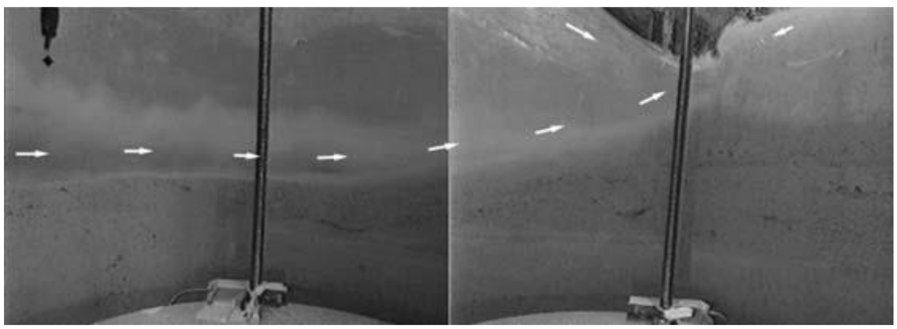

Figure 17: Example of Images Recorded from Inside the Cylinder (Tonkin et al. 2003)

Most observations made by Tonkin, et al. (2003) were taken from the video footage of the cameras located within the cylinder. The cameras were able to record the temporal formation of the scour hole and covered the entire contour of the cylinder at the level of the water/sand interaction. The observations of the scour mechanism are listed as follows:

- Wave strike and immediate breaking:
    - Horseshoe type vortex forms at the front of the cylinder, due to the overturning breaking motion of the wave
    - Scour hole forms, which is much deeper for the gravel substrate than for the sand
- Runup period:
    - Sand: scour at the front and sides of the cylinder causes the particles to become suspended and the sand is transported onshore, away from the cylinder
    - Gravel: scour at the front and sides of the cylinder causes the particles to move as bedload towards the back of the cylinder, where they settle into a uniform slope

- Early drawdown period:
    - Sand: very little scour at the back
    - Gravel: particles are entrained down the slope and are transported offshore by the force of a vortex sheet formed on the sides of the cylinder
- Final drawdown period:
    - Sand: a very turbulent horseshoe vortex forms at the back of the cylinder, which scours an important quantity of sand
    - Gravel: the scour hole formed in the previous stages is filled by gravel particles that were earlier transported onshore

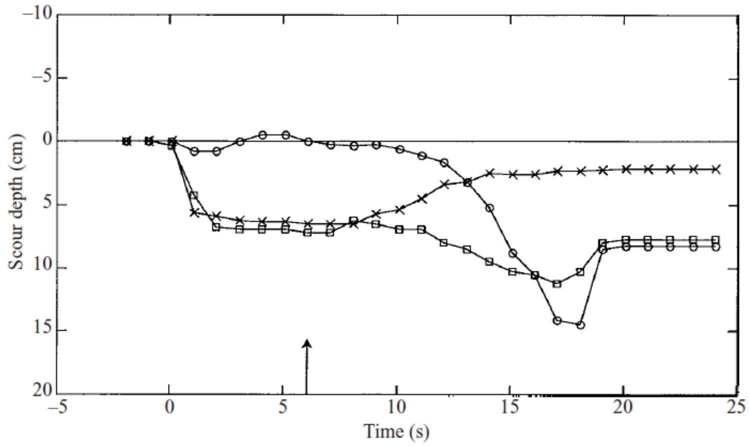

Figure 18: Time Development of Scour around a Cylinder on a Sand Bed (crosses: front, squares: sides, circles: back) (Tonkin et al. 2003)

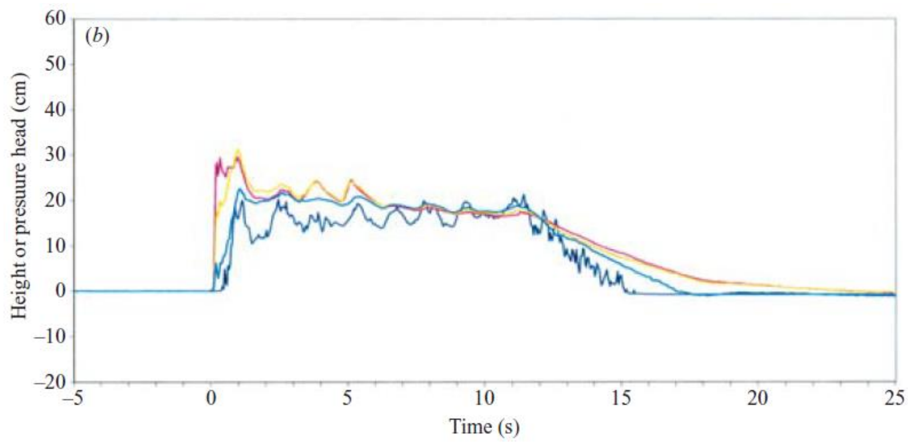

Figure 19: Wave Height (blue) and Pore Pressures (cyan, pink and yellow) at the Back of the Cylinder on a Sand Bed (Tonkin, Yeh, Fuminori, & Shinji, 2003)

In addition to this general scour mechanism, Tonkin, et al. (2003) also observed scouring effects caused by pore pressure gradients. They installed pore pressure transducers at the front, side and back of the structure below the initial level of the sand and at increasing depths, for intervals of 10 cm and up to 30 cm deep. These transducers measured a significant drop in pore pressure during the rapid drawdown period of the tests. Pore pressure drops were mostly measured for the tests with a sand bed. The drawdown period also coincided with the maximum scour depths at the back of the cylinder. The measured pore pressures indicated gradients reaching up to half of that required for liquefaction. Tonkin, et al. (2003) therefore concluded that the loss of sediment cohesion due to the pore pressure gradients caused the sand to be scoured more easily and were the main factor in the formation of the large scour hole behind the cylinder.

The study undertaken by Nakamura, et al. (2008) has both similarities and differences with the one by Tonkin, et al. (2003). Nakamura, et al. (2008) also chose to study the local scour around piers induced by tsunami waves, yet they focused on land- based structures. The setup used for the physical experiments consisted of a long sloped beach leading to a steep revetment. On the onshore side of the revetment, a horizontal sand bed was used as the foundation backfill for a 0.14 m wide wooden structure.

The test runs were performed using solitary and long-period waves. Both types of waves were generated using a piston-type wave maker. The duration of the long-period waves was approximately double that of the solitary waves. The parameters modified in the different runs included the still water depth, the incident wave height, the embedded depth of the structure, the wave period of the long waves, the widths of the structure (0.10 m and 0.14 m) and the median grain size of the sand particles (0.2 mm and 0.45 mm). Measurements were taken using capacitance type wave gauges, pore water pressure gauges and video cameras. For the 0.14 m wide structure, an alternate acrylic material was used, and thus a camera was placed inside the structure to record the scour formation at the offshore corner.

The scouring mechanism observed by Nakamura, et al. (2008) differed from that of Tonkin et al. (2003) mainly because of the different geometry of the structure and that there was no drawdown in Nakamura et al. (2008)’s experiments. They did observe that the runup of the waves caused a rapid flow along the sides of the structure and scour holes were created at both offshore corners of the structure. Along the sides of the structure, the flow was strong and sediment was brought into suspension and transported onshore. Once the flow velocities decreased and the scour hole had reached its maximum depth, deposition of the suspended sediment occurred. The sediment scoured on the sides of the structure also rolled down the steep slope formed during the uprush and slowly filled the scour hole at the corner of the structure. The final maximum scour depth was therefore observed to be only 75% to 90% that of the actual maximum scour depth.

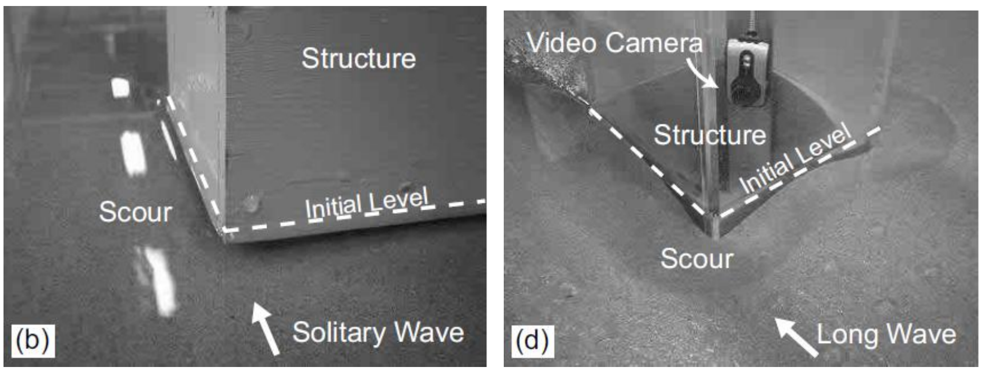

Figure 20: Video Images showing b) undermining of the corner of the structure and d) scour hole pattern (Nakamura, Yasuki, & Mizutani, 2008)

In addition to these observations, Nakamura, et al. (2008) also determined that the duration of the solitary waves was too short to properly simulate tsunami scour. In the case of the long-period waves, with wave period ranging from 6 to 14 seconds, the duration of the flow was long enough that the sand located behind the structure was also scoured. In cases where the embedded depth of the structure was small, the scouring was even able to undermine the offshore corner of the structure. The main conclusions of the study were that the final scour depth increases as the overtopping height increases, and that the maximum scour depth does not coincide with the final scour depth.

2.8 North American Design Guidelines

Finally, an aspect of literature that plays perhaps the most important role in the application of bore-induced scour mitigation methods is design guidelines. Most countries, as well as smaller regions such as provinces, states or cities, publish design guidelines for new constructions and rehabilitations. These regulation documents are generally tailored to the areas in which they are used. For example, design guidelines in Japan have numerous considerations for designs withstanding seismic loads and tsunami loads, which have a high frequency of occurrence in this country. In North America, tsunamis are much less common and so design guidelines will be less likely to include recommendations for tsunami mitigating designs. However, due to the increasing awareness of potential tsunami events in North America, a number of design guidelines are starting to incorporate sections specifically geared towards designing structures that can withstand tsunami loads and effects. The following section will present the current recommendations provided in these guidelines.

The City and County of Honolulu Building Code was the first design guideline in North America to provide recommendations for structures located in flood hazard districts, and more specifically potentially affected by tsunami waves. In article 11 of the building code, a subsection is reserved for the regulations pertaining to the location of structures with respect to coastal flooding boundary, potential forces and scour affecting the structural integrity of these building. Equations are provided for a number of tsunami-induced forces, which include the buoyant force, surge force, drag force, impact force and hydrostatic force. As for scour at structure foundations, only pier or pile type foundations are recommended for the coastal flood zones. Shallow foundations are not permitted, with exceptions for those protected by coastal structures or if located further than 300 feet (91.4 m) from the shore. As for estimations of potential local scour depths, a table is given in which the scour depth is provided as a percentage of the flow depth and for different soil types. These scour depth estimations were taken from the research of Dames and Moore (1980) (see Table 1).

The Federal Emergency Management Agency (FEMA) published a document in 2012 entitled "Guidelines for Design of Structures for Vertical Evacuation from Tsunamis". This design guideline provided the most up to date theory behind tsunami-induced forces, as well as design considerations for buildings being constructed specifically in coastal, tsunami prone zones.

An equation is provided for the estimated runup velocity of a tsunami wave on a beach. It is derived from the solution for the runup of an incident bore given by Shen and Meyer (1963). This equation takes into consideration the distance travelled by the bore on the beach. In order to take into consideration a beach with a non-uniform slope, the equation was modified slightly by Yeh (2006) to produce the following final form:

$$u_{max} = \sqrt{2gz_{max}\left(1 - \frac{z}{z_{max}}\right)} \tag{6}$$

Where u_{max} is the maximum propagation velocity of the bore, z_{max} is the maximum attained ground elevation and z is the ground elevation of the structure of interest. When examining a bore propagating over a horizontal surface, the maximum bore depth can be characterized as equation 7, thus leading to a final form of the velocity equation based on the maximum bore depth.

$$h_{max} = z_{max} - z \tag{7}$$

$$u_{max} = \sqrt{2gh_{max}} \tag{8}$$

The section reserved for the effects of tsunamis on local scour at the building foundations was relatively short in comparison to the sections focusing on tsunami induced structural loading. The same table as in the CCH, showing the scour depth estimations by Dames and Moore (1980) is provided.

Table 1: Dames and Moore Tsunami induced Scour Depth Ratios

Table 7-1 Approximate Scour Depth as a Percentage of Flow Depth, *d* (Dames and Moore, 1980)

Soil Type	*Scour depth (% of d) (Shoreline Distance < 300 feet)*	*Scour depth (% of d) (Shoreline Distance > 300 feet)*
Loose sand	80	60
Dense sand	50	35
Soft silt	50	25
Stiff silt	25	15
Soft clay	25	15
Stiff clay	10	5

Finally, the American Society of Civil Engineering is currently in the process of developing a chapter on tsunami loading and effects in their next edition of their standard entitled “Minimum Design Loads of Buildings and Other Structures”. A tsunami loads and effects subcommittee, composed of researchers and specialists in the subject matter, have been assembling observations and results of numerous field surveys in order to provide better recommendations for designing structures affected by tsunamis. The field surveys were performed in Japan, after the 2011 Tohoku tsunami. Evidence of local scour at building foundations was photographed at various locations along the affected coastline. The researchers noted that generally, local scour holes of the largest magnitude typically occurred at the corners of buildings where the water would have accelerated due to the obstruction. However, instances of scour were also observed at other shapes or types of structures, such as a bridge, a viaduct pier and a number of sea walls. There did not seem to be any correlation between soil type and scour depth. In addition, most scour depths were less than 3 m and resulted from a cycle of 2 to 3 waves of durations ranging from 40 to 60 minutes each. For each observation, the location, site features, flow depth, scour depth and soil type were recorded if possible. A sample of these survey results will be presented in Section 6. The ultimate goal of this collection of field surveys was to evaluate the current scour depth estimations provided in FEMA P646 (2012) and other models.

3. Experimental Investigation

3.1 Experimental Setup

The experimental investigations were conducted in the Large Flume of the Civil Engineering Hydraulics Laboratory of the University of Ottawa. The flume floor was made of concrete and its walls composed of concrete block, both of which were covered by a waterproof membrane. The flume has dimensions of 30 m in length, 1.5 m in width and 1 m in height, with a single pump at the upstream end. The following figure provides a top view and a side view of the flume layout, identifying key components and dimensions.

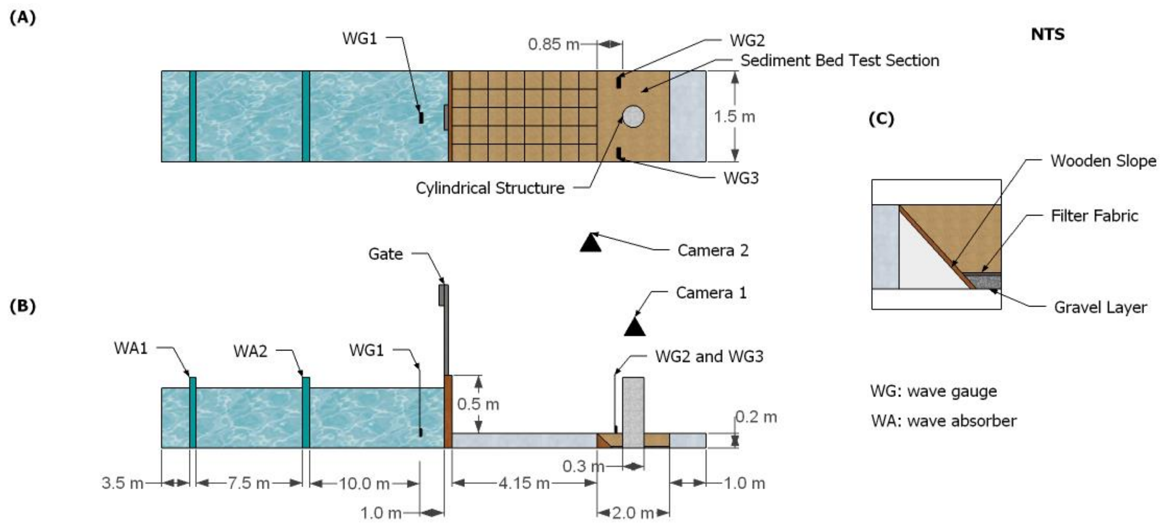

Figure 21: Experimental Layout (A) Top View (B) Side View (C) Detail of Floor and Sediment Bed Interface

In order to create a hydraulic bore, a composite steel and wood swinging gate, shown in Figure 22, was installed at a distance of 22 m downstream from the pump end of the flume. This gate, equipped with a lock and release mechanism, was used to impound a reservoir of water. The sudden release of the gate enabled the generation of a "perfect" hydraulic bore, in a similar way to that generated by a sudden dambreak. Rubber flaps installed on the sides and bottom of the gate were used to seal the seams. The gate was water tight for the majority of its seams, except for some minor leaks occurring in the two bottom corners of the gate. Within the gated reservoir side of the flume, two wave absorbers, shown in Figure 22, were installed in order to attenuate secondary waves within the reservoir. Initial tests indicated that these secondary waves were able to propagate to the farthest end of the reservoir, reflect off of the wall and cause fluctuations in the flow at the test section. The wave absorbers were composed of a vertical metal grid covered with a mesh material and spanning the entire width and height of the flume cross-section. These were installed at 3.5 m and 11.0 m from the pump end of the flume.

 

Figure 22: Left: Wood and Steel Framed Swinging Gate, Right: Wave Absorber

The test section was located in the portion of the flume downstream of the gate. An aluminum false floor with a height of 0.2 m was installed in this portion of the flume in order to provide a recess for the sediment bed. The false floor had a length of 4 m upstream of the sediment bed, and a length of 1 m at the downstream end of the bed. The upstream portion of the false floor was lined with a layer of sand, with a uniform grain size of 1 mm, in order to provide roughness. A grid, with dimensions of 20 x 20 cm, was also painted on this portion of the false floor for measurement purposes. Although the false floor had a perfectly horizontal surface after its initial installation, after the first test, the weight of the water caused the center of the floor to sag slightly. Therefore, any small amounts of water leaking from the gate would accumulate at the center of the floor. The effects of this imperfectly levelled floor and thin layer of water are further discussed in the Data Analysis section.

The sediment bed portion of the test section was 2 m long and delimited at each end by the false floor sections. A cylindrical structure with a diameter of 0.3 m made of Plexiglas was located in its centre. The structure was fastened to a large wood board positioned on the flume floor. The base of the sediment bed was composed of a layer of course gravel, of approximately 3 cm thick covered by a layer of filter fabric. This layer provided drainage for any water that infiltrated below the false floor and which eventually reached the sediment bed. At each upstream and downstream interface of the sediment bed with the false floor a wood ramp of 35° was installed (Figure 21C). These ramps minimized the inevitable local scour that would occur at this interface and possibly have an effect on the flow characteristics. Finally, the sediment bed was filled with two types of uncompacted sediment. Both coarse sand and pea gravel were used, with uniform grain size diameters of 1 mm and 1 cm, respectively. Two images of the sediment bed are pictured below.

Figure 23: Left: Sand Bed, Right: Gravel Bed

3.2 Scaling

Initially, scaling was not considered for the structure's size and the bore depths.   The structure used in all tests was selected based on its circular shape and also because it had been used by Al-Faesly et al. (2014) in their experiments on tsunami impact forces on structures. Thus, results of the scour experiments could in future be combined with the results of the impact forces experiments for further analysis. The bore depths were very much dependant on the water depth in the reservoir. Because of the upper height limit of the flume wall and the lower height limit of the false floor, a range of water depths between these two limits were chosen. An initial set of experiments were carried out without the sediment bed in place in order to verify that the selected water depths produced fully broken bores by the time they had reached the end of the false floor. The most important scaling factor for these experiments was the Froude number of the bores. These could only be determined after each test and are further discussed in the Results section.

As for the selection of the sediment types and sizes, availability of material was once again a limiting factor. Also, in order to improve comparability of the results with previous similar experiments, the decision to perform tests with both sand and gravel was made. Analytical calculations were performed prior to selecting the sediment grain sizes in order to determine the critical velocity for initiation of sediment motion. First the critical shear stress was computed for the possible grain sizes, using equation 9 below. The entrainment function was computed using Van Rijn's formula based on the Shield's diagram, equations 10, and using equation 11 to determine the dimensionless particle size parameter. Assumptions were made for the density of the particles, taken as 2650 kg/m^3 and the density of water, taken as 998.2 kg/m^3 at 20°C.

$$\tau_{cr} = F_s(\rho_s - \rho)gD \tag{9}$$

$$F_S = {0.013}\big/{D_{gr}^{0.29}} \quad for\ 0.001 \leq D \geq 0.005$$
$$F_s = 0.056 \qquad for\ 0.07 \leq D \geq 0.03 \tag{10}$$

$$D_{gr} = D\left(\frac{g\left(\left[{\rho_s}/{\rho}\right] - 1\right)}{\upsilon^2}\right)^{1/3} \tag{11}$$

In order to compute the critical flow velocity for initiation of particle motion, the Chezy formula, equation 12, was combined with the equation for shear stress, equation 13. The resulting formula, equation 14, provided the required estimates of critical velocity for the possible sediment grain sizes. Once again, certain assumptions applied. The Manning's roughness used in the Chezy coefficient was estimated based on the suggestion from the US Geological Survey (Aldridge and Garrett, 1973) for an array of different grain sizes in order to assess the potential for sediment motion. The flow depth used in the hydraulic radius was taken as 0.25 m to account for a larger bore depth.

$$v = C\sqrt{RS_0} \tag{12}$$

$$\tau_0 = \rho g R S_0 \tag{13}$$

$$v_{cr} = C\sqrt{\frac{\tau_{cr}}{\rho g}} \tag{14}$$

The results of this analysis, shown in the table below, demonstrated that the expected bore front celerities would be sufficient for sediment motion. For the sand particles of 1 mm, the required velocity is 0.21 m/s and for the gravel particles of 1 cm, the required velocity is 0.77 m/s.

Table 2: Critical Velocity for Initiation of Sediment Motion

Particle Diameter (m)	Critical Shear Stress (N/m^2)	Critical Velocity (m/s)
0.001	0.53	0.21
0.002	1.30	0.34
0.005	4.25	0.58
0.007	6.42	0.67
0.01	9.17	0.77
0.015	13.75	0.89
0.02	18.33	0.99
0.03	27.50	1.18

3.3 Instrumentation

The instrumentation used during the experimental tests included wave gauges and digital video cameras. Three capacitance type wave gauges with an accuracy of 0.4% were used to record the time-history of the water surface elevation at different locations of the experimental layout (Figure 21). Before installing them in the model, the gauges were calibrated in a barrel outside of the test area. They were calibrated for water depths of 0 to 70 cm. The calibration curves are shown in Appendix A. Two wave gauges were positioned on either side of the pier structure at 20 cm from the flume walls and 15 cm upstream of the leading edge of the cylinder. These wave gauges were used to record the time-history of the bore depth over the duration of the test. The third wave gauge was positioned behind the gate, in the reservoir, at a distance of 1.0 m from the gate and 1.2 m from the flume wall. This wave gauge was used to record the time-history of the water surface elevation within the reservoir over the duration of the test.

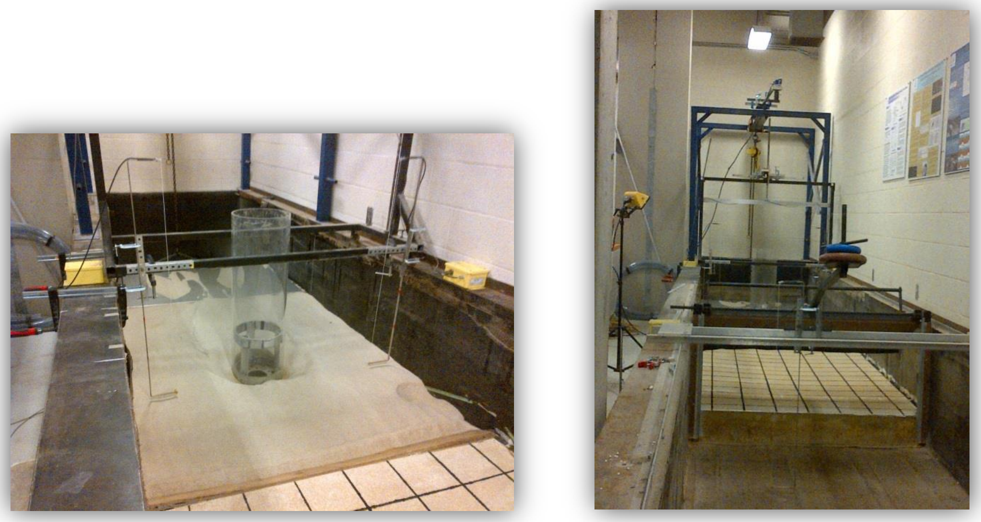

Figure 24: Left: Two Wave Gauges at Structure, Right: Wave Gauge in Reservoir behind Swinging Gate

Two digital video cameras were also used during the experimental investigations, pictured in Figure 25. The first one, a regular digital camcorder, was positioned directly above the structure with a vertical view point looking down at the structure and the closely surrounding sediment bed. This camera was used to qualitatively observe the development of the scour and the changes in flow directly at the structure. The second digital video camera was a high-speed camera, with a maximum frame rate of 1000 fps and a resolution of 1280x1024. This camera was located at a much higher elevation over the test section. The view point of this camera was also a downward looking vertical image, with its center aligned with the interface between the false floor and the sediment bed.

Figure 25: High Speed Video Camera and Regular Video Camera

This high-speed digital video camera had a dual purpose. The first was to track the propagation of the bore front as it moved downstream towards the structure, in order to estimate the instantaneous and average bore front celerities. The second use of the high speed video camera was for Particle Tracking Velocimetry (PTV). Before starting each test, four small Styrofoam balls were placed in the reservoir at approximately equal intervals from each other and in proximity to the swinging gate. During the test, these Styrofoam balls were easily captured by the high speed video camera as they travelled towards the structure on the surface of the water. Because these particles travelled through the camera view after the initial bore front had passed, they were used to estimate the temporal velocity of the ensuing sustained flow.

Finally, the instrumentation used to measure the final local scour around the structure at the end of each test was a Disto™ laser altimeter with a precision of ± 1.00 mm. The laser scour measurements were taken once the surface of the sediment bed had dried and only the final scour depths remained. Elevation measurements were taken over the entire surface of the sediment bed using a grid spacing of 5 cm x 5 cm and with a reference height equal to that of the false floor. These elevations were then mapped using GIS software and an inverse distance weighted interpolation scheme was applied in order to better represent the final bathymetry around the structure.

3.4 Testing Procedure and Program

Once all instrumentation was in place and the sediment bed was levelled, the reservoir was slowly filled with water to the desired depth, and the flume pump was turned off. The initial conditions in the reservoir were zero initial flow with the impoundment depth shown in Table 3 for the various test cases. Downstream of the gate, initial conditions were dry bed with no flow. The gate was then manually unlocked and quickly opened, its swinging movement being aided by a counterweight. The bore then propagated over the false floor and finally over the sand bed, while all measuring devices were recording. When the reservoir was completely empty, the test was complete. Finally, when the surface of the sediment bed had dried, the laser altimeter measurements were taken.

Table 3: Test Schedule

Test Number	Sediment Type	Reservoir Depth (cm)	
		Above Flume Floor	Above Bed
1	Sand	64.3	44.3
2	Sand	39.4	19.4
3	Sand	36.5	16.5
4	Sand	33.4	13.4
5	Gravel	66.8	46.8
6	Gravel	56.8	36.8
7	Gravel	50.9	30.9
8	Gravel	48.8	28.8
9	Gravel	45.2	25.2
10	Gravel	56.3	36.3

The opening time of the gate was recorded using the video cameras and verified using the Lauber-Hager criterion, described in the Literature Review (Section 2). Snapshots of the gate in its closed and opened position were taken, as shown in the images below. The opening time was then calculated using the number of frames between the snapshots and the frame-rate of the video camera. This opening time could then be substituted in the Lauber-Hager criterion equation in order to verify that the expression was less than the square root of two.

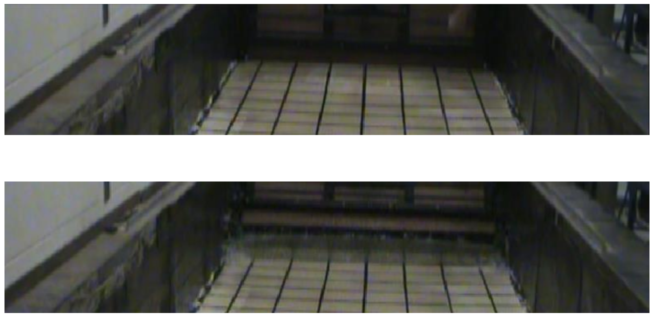

Figure 26: Successive Snapshots of Gate Opening

The experimental program consisted of two sets of tests. Each set had a different sediment type, either sand or gravel, and employed different reservoir depths. Table 3 shows all of the tests completed in this research program. A total of four tests were conducted using sand while six others used gravel. Sand tests consisted of three regular tests (test 1, 2 and 3), with progressively decreasing water levels. One additional special test was conducted using sand, (test 4) in which the scoured bed resulting from test 3 was subsequently flooded and a secondary wave was generated over this flood level. The gravel tests used the same progressively decreasing water levels used for the sand tests. Test 10 was a repeat of test 6 in order to verify the repeatability of the test results.

4. Data Analysis

4.1 Bore Depth

The temporal history of the bore depth and the time history of the water surface elevation in the reservoir were recorded for each test using the three wave gauges described in Section 3.3. The gauge located behind the gate in the reservoir was used to provide an exact reading of the reservoir depth before the start of each test. Figure 27 shows the wave gauge results for Test 10. In this graph, the first wave gauge (WG1) was located in the reservoir. The water surface elevation was therefore constant until the gate is opened, at which point there is a sudden vertical drop in water surface elevation. In addition to the initial reservoir depth, this gauge also provides a time history of the decreasing water surface elevation in the reservoir over the duration of the test. This was especially useful in the early stages of the experimental design. Fluctuation in the reservoir water surface elevation indicated the presence of secondary waves propagating in the reservoir. These waves could have had an effect on the bore depth, and so with the installation of the two wave absorbers, the fluctuations in the reservoir were sufficiently minimized.

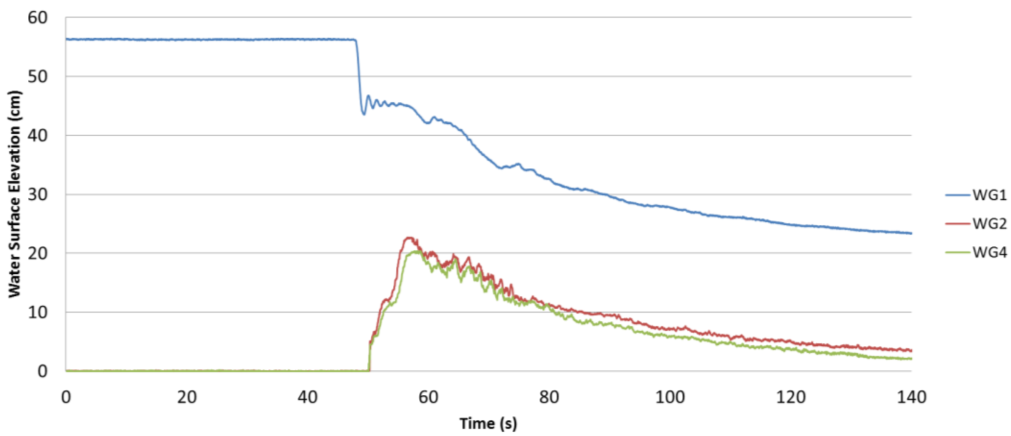

Figure 27: Time History of Water Surface Elevation
Test 10 (Gravel, 56.3 cm Reservoir Depth)

The remaining two wave gauges were located on either side of the structure over the sand bed. Their results in Fig. 27 above are indicated as WG2 and WG4. This time history of the bore depth shows that the bore front was almost vertical, as expected in a naturally occurring bore. The bore propagated over the false floor and reached the structure within less than 4 seconds of the gate opening. The bore reached a maximum depth in the first 10 seconds of the test, after which its depth gradually declined for the remainder of the test. In Test 10, as well as in all of the other tests, there is a small difference in the bore depth readings of the two wave gauges located at the structure. These differences may be attributed to nonuniform water surface elevations caused by the uneven local scouring of the bed on either side of the structure.

Finally, the time histories of the bore depths for different tests were compared in order to assess the similarity of the experimentally generated bores. As shown in Figure 28, the initial bore fronts had a vertical profile with maximum bore depths being attained within 10 seconds. The rate of decline of the bore depth was greater for the larger bores due to the higher initial water surface elevation in the reservoir. The differences in maximum bore depth also become greater with increasing reservoir depths. The full results of time history of bore depth and water surface elevation in the reservoir for each test are provided in Appendix B.

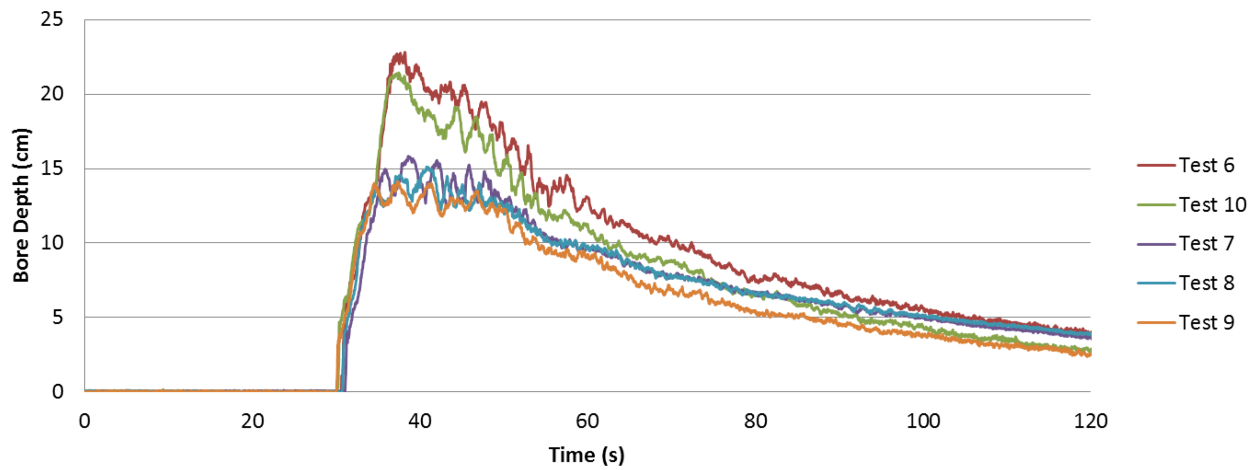

Figure 28: Time History of Bore Depths for a Sample of Tests

4.2 Bore Front Celerity

The propagation of the bore fronts across the false floor and the sediment bed was tracked using the high speed video camera and the celerity of the bore fronts was estimated using two methods. From the videos, still images of the bore front at different distances along the downstream test section were taken. The distance travelled by the bore front from one image to the next was measured using the gridlines that were painted on the false floor.

The first method of calculating the bore front celerity was an exact method, in which the real shape of the bore was tracked. In the figure below, the dashed blue line delineates the bore front from the previous image, whereas the solid blue line delineates the bore front in the current image. In all figures, the spacing of the grid lines is 20 cm. This method provided results of instantaneous celerities. The tracking of the real bore front permitted the capture of outbursts and therefore provided a wide range of celerities. These included both the maximum and minimum celerities attained by the bore front.

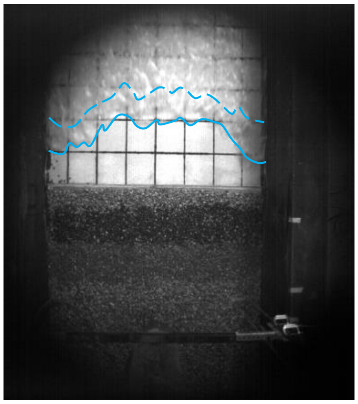

Figure 29: Video Snapshot for Exact Method of Bore Front Tracking

The second method of analysis used tracked the approximated shape of the bore front. As shown in Figure 30, the shape of the bore front was approximated as an arc, drawn in red. Calculating bore front celerities using this approximate shape provided better results of average bore front celerities over the width of the flume. The distinct arced shape of the bore front is a result of the imperfect false floor. Due to the slight sag and minimal water accumulation at the center line of the false floor, the propagation of the bore front was slowed down in its center. However, once the bore front reached the sediment bed, the increase in bed roughness cause the bore front to reassume a linear shape.

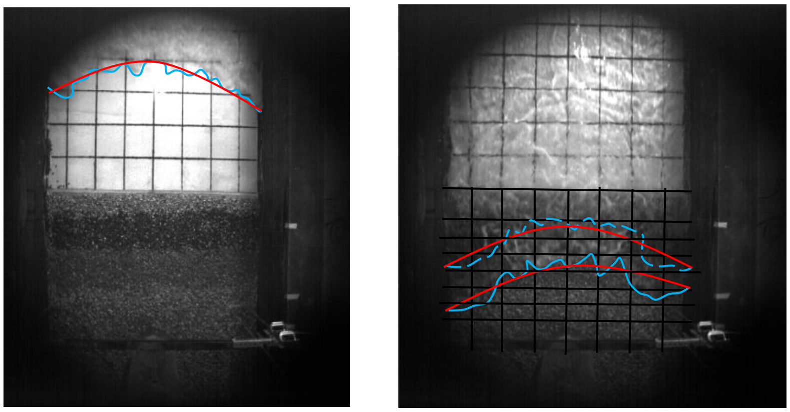

Figure 30: Video Snapshot for Average Method of Bore Front Tracking

4.3 Sustained Flow Velocity

The method used to calculate the flow velocity from these Styrofoam balls is known as particle tracking velocimetry, as used by Orendorff et al. (2011) in the analysis of flow velocity through an embankment dam breach. Still images of the videos were taken at different times during the test and the distance travelled by the particles between these snapshots provided their velocity. Because multiple particles were used and because they passed through the camera view successively over the course of the test, the variation in flow velocity could also be estimated. The following image shows a still image of the Styrofoam particle, circled in red, taken by the high-speed video camera.

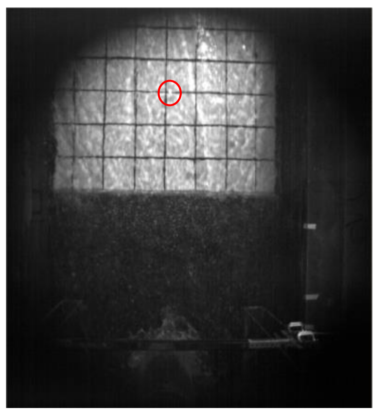

Figure 31: Video Snapshot for Particle Tracking

Corrections were applied to the distances travelled by the particles in order to compensate for the camera viewpoint and the depth of the flow. Because the position of the particles was measured based on the grid lines, their lateral separation at the bottom of the flow appeared greater than the actual position of the particles floating on top. The figure below illustrates this phenomenon as well as the variables used in the correction equation. The distance between the particles, D_P, was calculated based on the adjusted distance between the gridlines, D_L, using the ratio of the height of the camera, H_C, to the height of the water, H_W.

$$D_P = \left(\frac{H_C - H_W}{H_C}\right) D_L \tag{15}$$

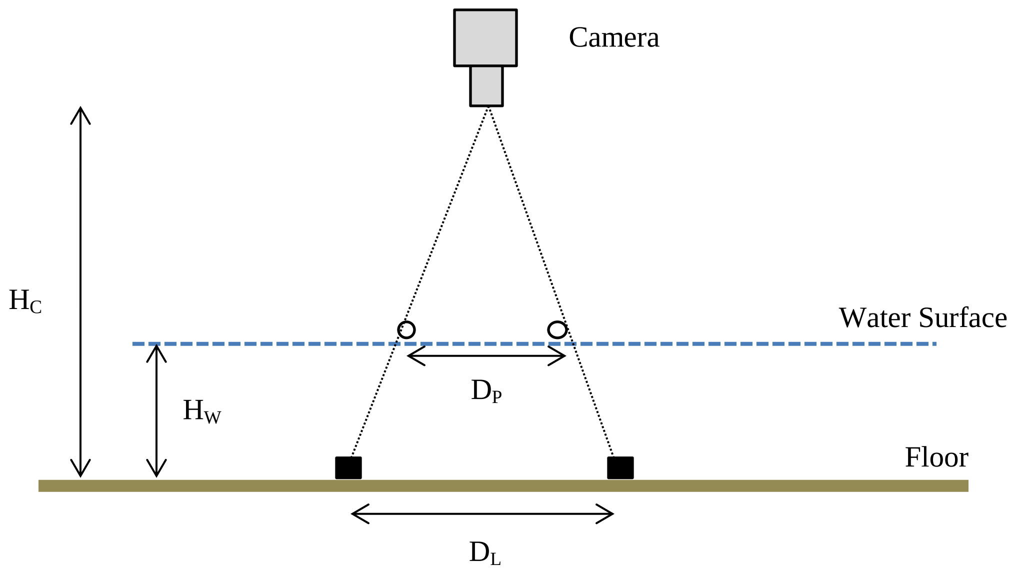

Figure 32: Illustration of Camera Correction for Particle Distances

4.4 Sediment Bed Elevations

The final elevations of the scoured sediment bed were measured using a laser altimeter. Point measurements were taken over the entire sediment bed surface at a grid scale of 5 cm. These measurements were then zeroed based on the average elevation of the false floor on either side of the sediment bed. In order to provide a better visualization of the final scour depth magnitudes and locations, the point measurements were interpolated over the sediment bed area using GIS. The interpolation used was inverse distances weighted with a maximum range of 5 cm. Figure 49 in Section 5.3 shows the final scour plots for each test. The scale was selected based on the natural breaks in the data. This scale therefore better captured the sudden changes in elevation and emphasized important boundaries such as the edge of the main local scour hole. In addition to the scour plots, cross-sections of the sediment bed were also plotted. A selection of these cross-sections is provided in Appendix C.

5. Results

5.1 Bore Characteristics

The first set of results that will be discussed are the bore characteristics, such as the bore front velocities, the sustained flow velocities and the bore depths, as well as certain relationships derived from these, such as the Froude number. The relationship between the maximum bore depths and the reservoir water depths was linear, as shown in Figure 34 below. This linear relationship has a slope of 0.72 and a correlation of 95%. The difference in bore depth for Tests 6 and 10, of 2.4 cm, is high considering the reservoir water depth only had a difference of 0.5 cm. This provides an estimate of experimental variability. Interestingly, the maximum bore depth for Test 1 was higher than that of Test 5, even though the reservoir water depth was the highest for the latter. This may have been caused by the sediment type. In the case of Test 5, the roughness of the gravel may have slowed the bore down and caused a dissipation of the water depth before the bore reached the wave gauge.

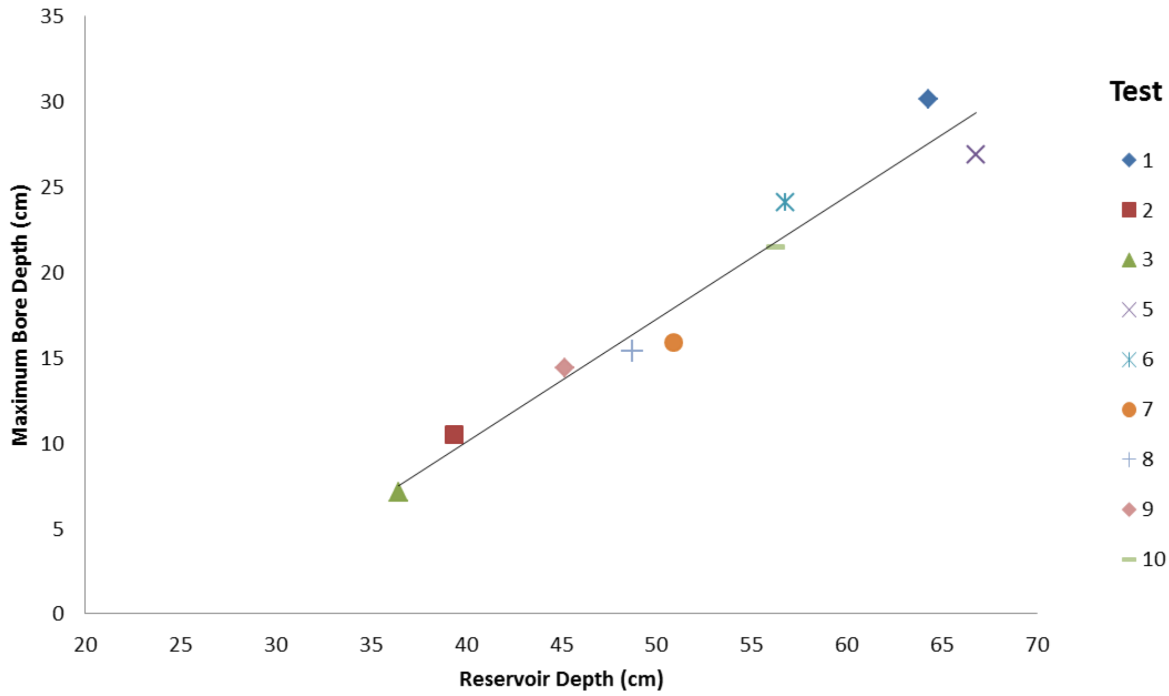

Figure 33: Relationship of Maximum Bore Depth to Reservoir Water Depth

A comparison of the measured time history of the bore depths to one derived from theory is presented below for Test 2 on sand (Figure 34) and Test 9 on gravel (Figure 35). In order to plot the theoretical bore depth time history, the measured time history of the reservoir water depth was used in conjunction with Stoker's equation for a sudden dam break. Equations 1 and 2 from Section 2.1 of the literature review were combined to form a time dependant expression relating the bore depth to the reservoir depth at a given location. The resulting bore depth represents the theoretical solution taking into consideration the same temporal decrease in reservoir water depth as for the observed results. In both cases, the observed bore depth is greater than the theoretical bore depth. This is due to the roughness of the sand floor and sediment bed, causing an increase in bore depth. In Stoker's equation, a smooth downstream surface is assumed. Evidence of the effect of the bed roughness on the bore depth is also present when comparing the results of the sand test to those of the gravel test. In the case of the sand, the difference between the theoretical bore depth and the observed bore depth is on average 5 cm in the first 20 seconds, whereas for the gravel test this difference is of 7 cm.

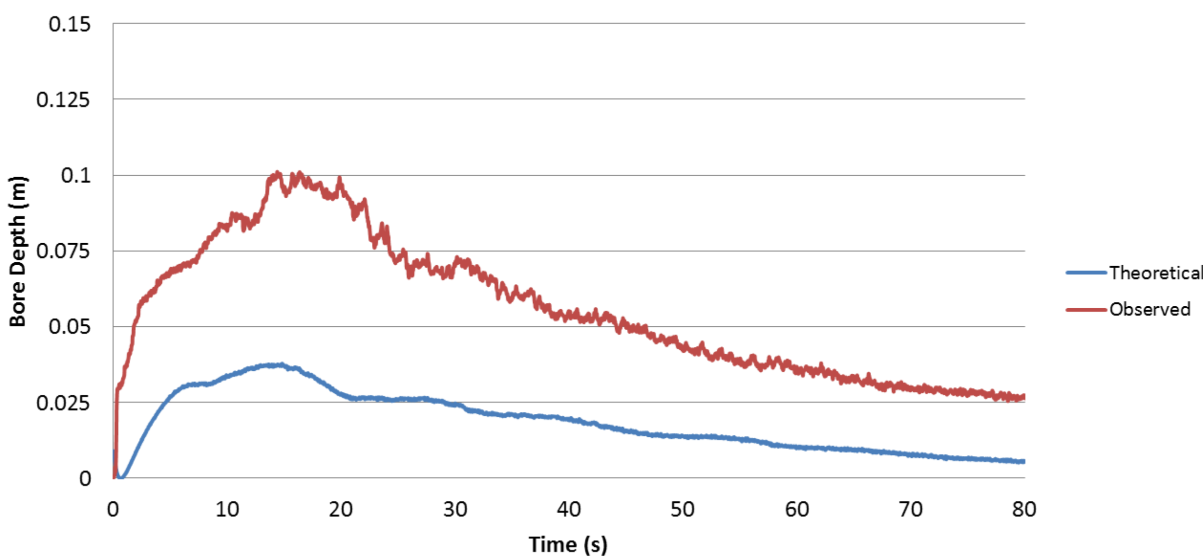

Figure 34: Comparison of Time History of Bore Depth to Theory for Test 2

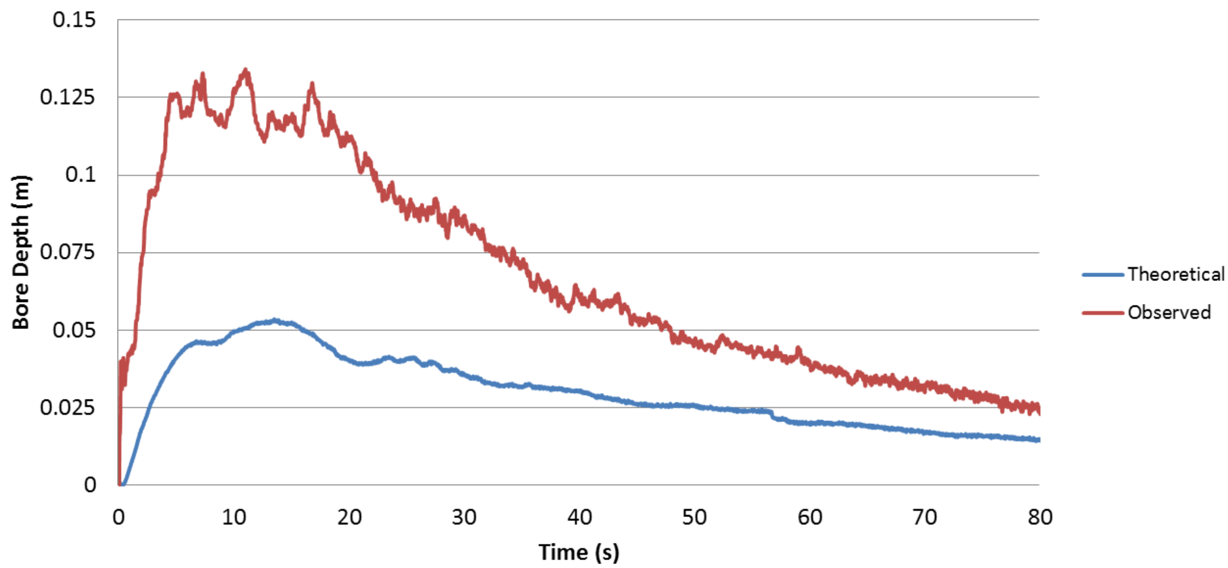

Figure 35: Comparison of Time History of Bore Depth to Theory for Test 9

The bore front velocity results are presented as instantaneous bore front velocity, calculated using method 1, and average bore front velocity, calculated using method 2. The instantaneous bore front velocity results indicated a wide range of velocities were achieved by the bore front as it travelled across the false floor and the sediment bed. In general, the highest velocities were recorded at locations closest to the gate and the lowest velocities were recorded closest to the structure. The maximum instantaneous velocities recorded were caused by localized bursts and reached as high as 3.92 m/s. At the structure location, the instantaneous velocities reduced significantly and were in the range of 0.3 to 1.3 m/s.

The average bore front velocities provided a better estimate of the flume width averaged velocity of the bore, and are shown in Figure 36 for five of the test cases. In this case, the range in velocities was lower than for the instantaneous velocities, with average velocities over the length of the test section of 2.16 to 1.15 m/s. For the tests with higher reservoir water depths, the bore front velocities gradually decreased as the bore approached the structure, as shown in the figure below. On the other hand, for the tests with lower reservoir water depths, the bore front velocities remained constant as the bore travelled across both the sand floor and sediment bed.

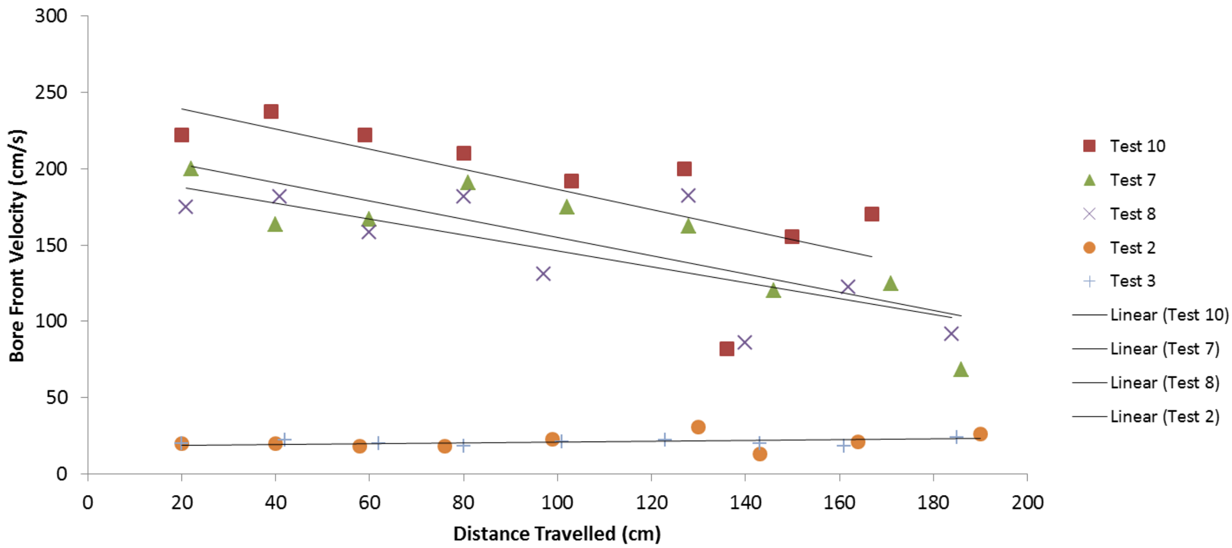

Figure 36: Average Bore Front Velocity over Distance Travelled by the Bore

The average bore front velocities can also be plotted against the maximum bore depths. In this case, the average bore front velocities were taken as the flume width averaged velocity at the location of the interface between the false floor and the sediment bed. Taking these velocity values ensures that the bore front velocity has not yet been affected by the change in roughness at the sediment bed. The results of this relationship are shown in Figure 37. In general, the bore front velocities increase at a constant rate with the increasing maximum bore depths, with the exception of Test 9 which had a lower bore front velocity. These results were also compared with the theoretical relationships proposed by various researchers and in some design guidelines. Figure 38 shows that the results of the current tests resemble very closely those obtained by the equation proposed by FEMA P646 (2012). This equation, introduced in the literature review, relates the bore velocity to the square root of 2g times the bore depth.

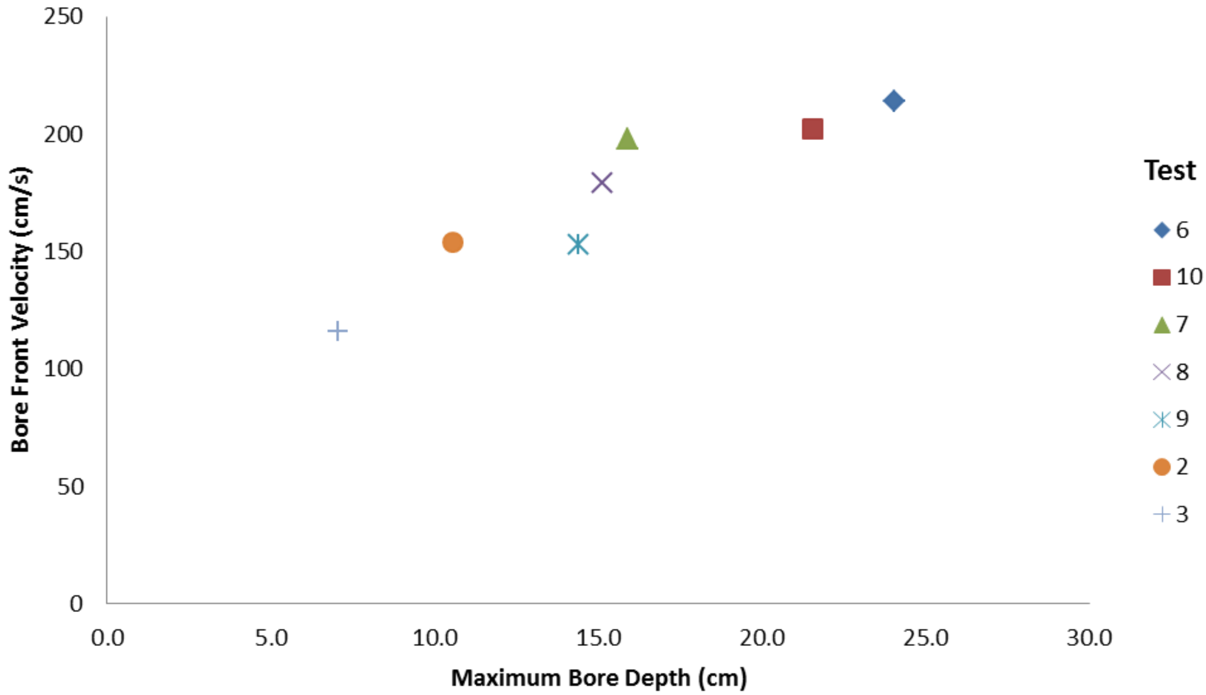

Figure 37: Relationship of Bore Front Velocities to Maximum Bore Depths

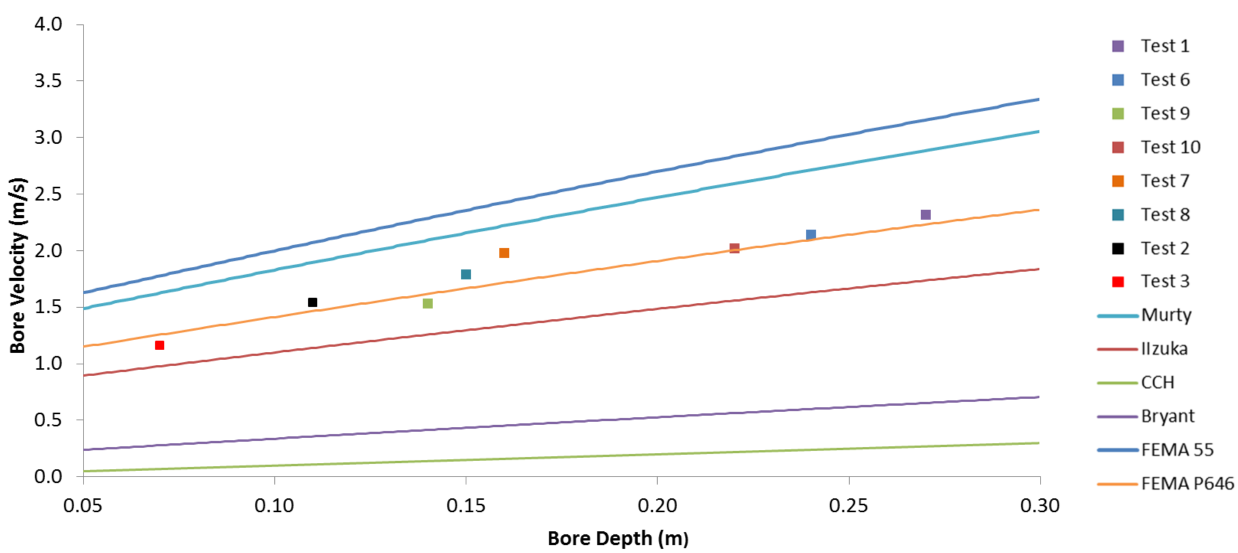

Figure 38: Observed and Theoretical Bore Velocity/Depth Relationships

Finally, the last set of results pertaining to the bore characteristics are the Froude numbers of the bores. As was observed by Chanson and Khezri (2012), fully broken bores occur when the Froude number exceeds values of 1.3 to 1.4. Therefore, in the present study, it was crucial that the bores attain Froude numbers close to these values upon reaching the end of the false floor, before travelling over the sediment bed test section. The following table provides the maximum bore depths, bore front velocities and Froude numbers for each test at this location. In all cases, except Test 9, the Froude numbers are well over 1.3, thus indicating that they were fully broken. In the case of Test 9, the Froude number falls just short of the lower Froude number limit of 1.3. This is due to the lower bore front velocities recorded for this test.

Table 4: Bore Froude Number Results

Test	Max Bore Depth (m)	Average Bore Front Velocity at End of False Floor (m/s)	Froude Number
6	0.24	2.14	1.39
10	0.22	2.02	1.39
7	0.16	1.98	1.59
8	0.15	1.79	1.47
9	0.14	1.53	1.29
2	0.11	1.54	1.51
3	0.07	1.16	1.39

Results of the particle velocity analysis provided estimates of velocity for the sustained flow that persisted once the bore had passed. Up to four particles were tracked for a sample number of tests and their velocities were calculated much in the same way as the bore front velocities. The sustained flow velocities ranged from 201.5 to 75.2 cm/s and the particles were spaced from 0.46 to 9 seconds apart. The first figure below shows the average particle velocity over the elapsed time of the particle tracking for each test. As a general trend, the particle velocities decrease over time, indicating that the sustained flow velocity, as well as flow depth, decrease over time. In Figure 40, the actual flow deceleration was calculated for each test and a clear relationship between the reservoir water depth and the sustained flow deceleration is present.

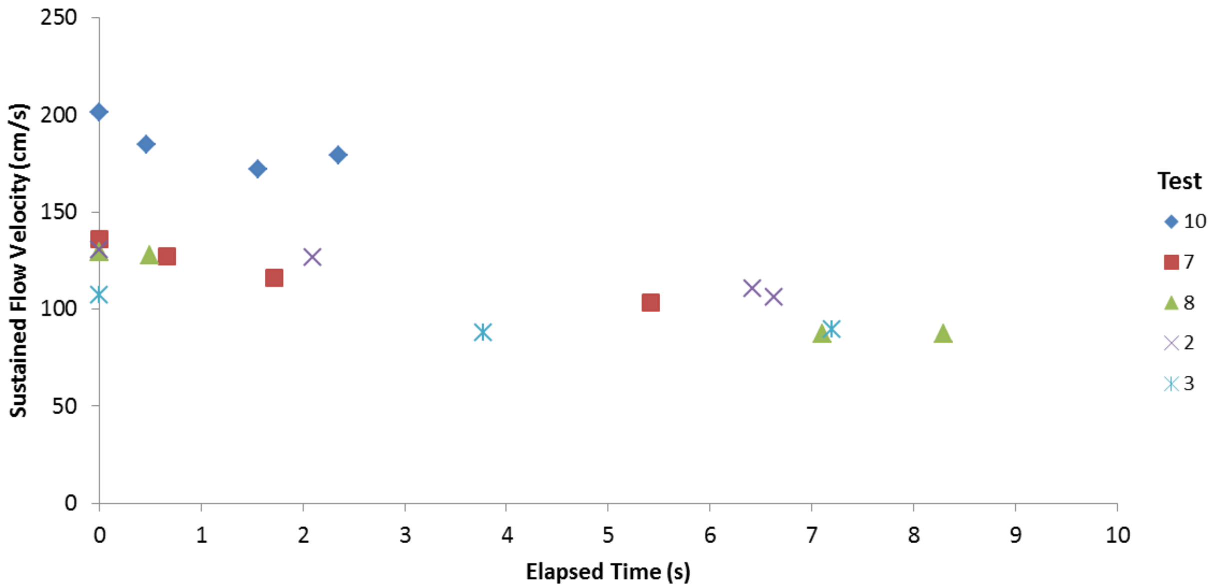

Figure 39: Time History of Sustained Flow Velocities

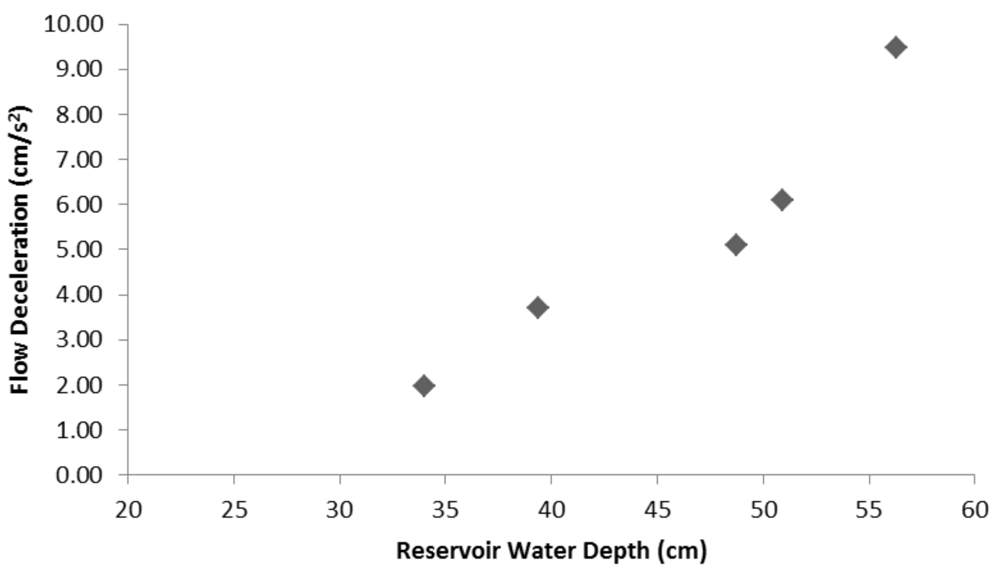

Figure 40: Relationship between Sustained Flow Deceleration and Reservoir Water Depth

5.2 Observed Scouring Process

From the video camera located directly above the structure, recordings of the scouring process around the structure were captured. These recordings provided a better understanding of the local scouring process for the two different sediment types and for the unique flow regime of the bore. The images captured from these videos show the structure from above, with the flow propagating from left to right.

For the tests with larger bore depths, ranging from 20 to 35 cm, the initial impact of the bore with the structure caused the water to form an area of very high turbulence directly in front of the structure, which lasted less than 5 seconds. This area, shown in the image below, was characterized by water being pushed vertically upwards along the structure front and falling back onto the water surface a few centimeters upstream of the structure. Below this zone of upper turbulence is where a horseshoe vortex would form and begin scouring the sediment at the front of the structure. At the same time, a zone of turbulence was also formed at the back of the structure in the form of a streamwise jet. This jet was most likely caused by the submerged flow at the sides of the structure, resurfacing at this location directly behind the structure.

Figure 41: Initial Bore Impact on Structure (Test 5, 8 sec.)

The zone of turbulence then began to dissipate as secondary waves caused by the structure obstruction began to propagate upstream away from the front of the structure. Figure 42 shows these waves which persisted and weakened until the flow had become significantly less turbulent after approximately 10 to 15 seconds. The jet at the back of the structure enlarged, taking a conical shape still originating at the center of the structure.

Figure 42: Dissipation of Turbulent Flow at Front of Structure (Test 5, 13 sec.)

Finally, the flow upstream of the structure lost most of its turbulent nature and the boundaries of the local scour hole were visible. As shown in the image below, the flow entered the scour hole at the front of the structure and followed the sides of the structure as it flowed downstream. The greater part of the back of the structure, stretching across almost a third of the circumference of the cylinder, was at this point producing vortices and a turbulent flow coming off of the structure.

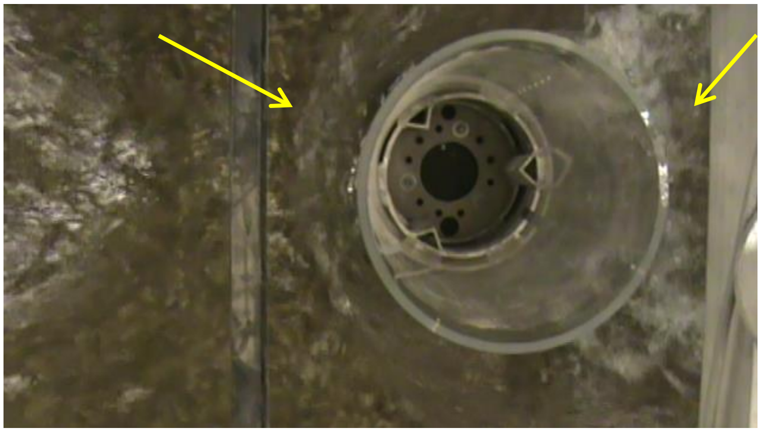

Figure 43: Stabilized Flow for Large Bore Depths (Test 5, 28 sec.)

For the tests with smaller bore depths, ranging from 5 to 20 cm, the initial turbulence caused by the bore impact did not occur. The secondary waves propagating upstream and caused by the structure obstruction dissipated quickly, as shown in the image below. The turbulence at the back of the structure was very minimal or not present at all. The flow lost its turbulent characteristics quickly, behaving more like a sustained supercritical flow.

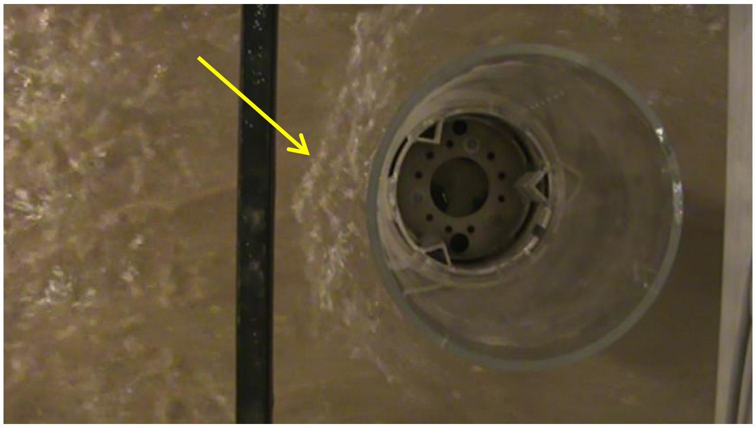

Figure 44: Typical Flow for Low Bore Depths (Test 3, 4 sec.)

Differences in the scouring process between the sand and gravel beds were also observed in these recordings. In the case of the gravel beds, as the bore first flowed over the sediment bed, the less turbulent zone upstream of the structure, pictured below, allowed for the observation of sediment transportation. Gravel particles could be seen being dislodge and entrained in the flow, travelling downstream into the more turbulent areas. This indicated that scouring of the entire sediment bed occurred in addition to the local scouring at the structure foundation.

Figure 45: Gravel Particle Movement as Bedload (Test 5, 11 sec.)

In the cases with the sand bed, the boundaries of the local scour hole were visible and easily identifiable early on in the tests. The recordings therefore captured the increase in size of the local scouring hole as the duration of the test progressed. The images below show snapshots of the scour hole for Test 3 at 5 second intervals. These observations were only visible for Tests 3 and 4. In the case of Test 1, the point at which the scour hole reached the bottom of the sediment bed was visible in the recording. As shown in Figure 47, the contrasting colours of the sand and the black filter fabric clearly indicated that the scour hole had reached the bottom of the sediment bed at the front of the structure.

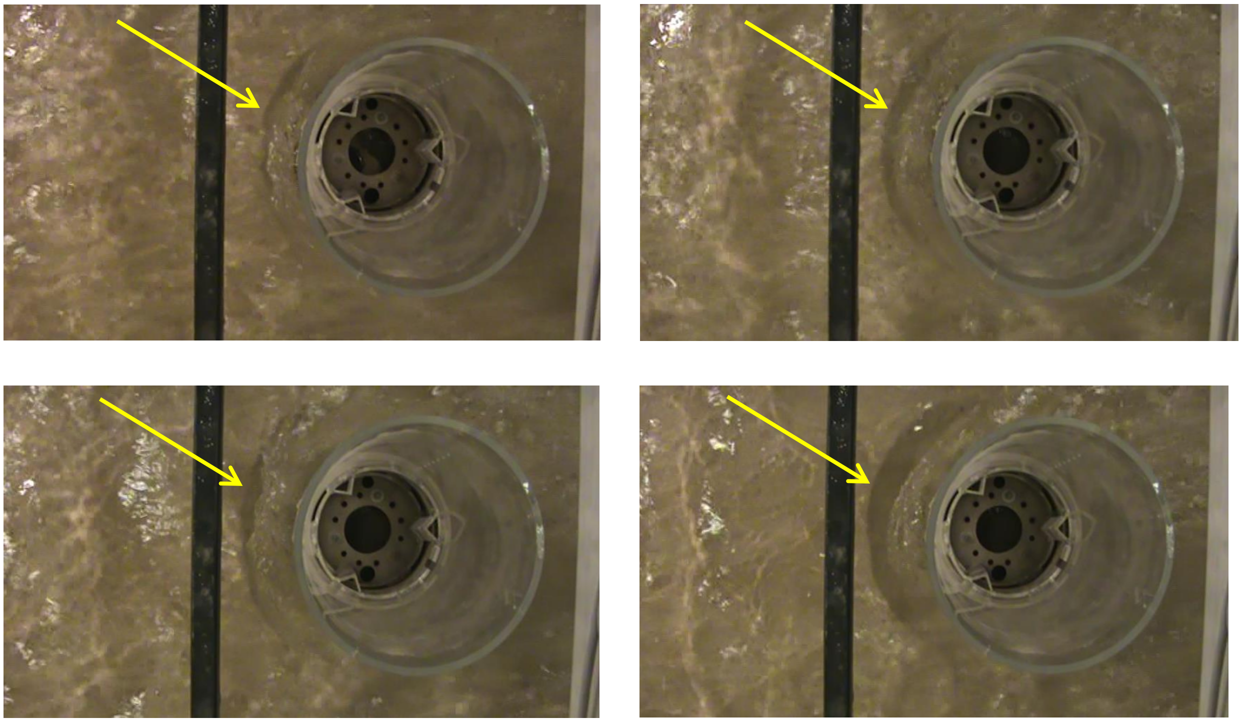

Figure 46: Temporal Formation of Local Scour Hole in Sand at 5 second Intervals (Test 3)

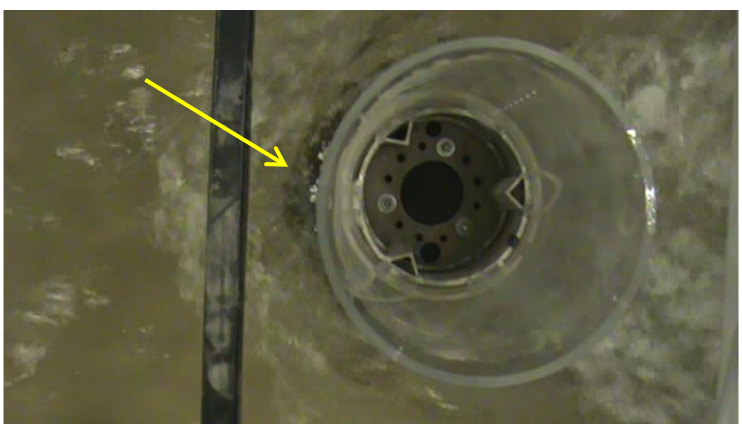

Figure 47: Bottom of Sediment Bed Visible in Scour Hole (Test 1, 25 sec.)

5.3 Final Local Scour Characteristics

The scour plots presented in Figure 48 provide the final sediment bed elevations after each test. The green, yellow and orange areas represent scour, whereas the pink and white areas represent deposition. In some cases, the scour depth was so great that it reached the bottom of the sediment bed, as indicated by the black areas. The local scour holes formed by the bores were for the most part semi-circular in shape with the maximum scour depth occurring along the upstream sides of the structure. The scour depth then decreased linearly towards the upper most edge of the hole. In all cases, there was also an area of deposition at the back of the structure.

For the tests with a sand bed, the first bore depth, Test 1, very quickly created a large scour hole that hit the bottom of the flume before all the water in the reservoir was depleted. In this test, the final scour depth at the front of the structure was of a similar magnitude to the scour depth at its sides. However, the total scouring process was incomplete, as the back of the structure was not scoured to the same degree as the front and the sides. In the case of Tests 2 and 3, the scouring process did not develop to the same degree as in Test 1 and the local scour hole depth at the front of the structure was smaller than that at the sides of the structure. This incomplete scouring process can be attributed to the natural short duration of the bores.

In the case of Test 1, the bore depth and velocity had important magnitudes such that a significant amount of the surrounding sand bed was scoured. The scour along the upstream and downstream edges of the sand bed were caused by the transition between the sediment and the false floor. The two angled areas of scour propagating from the back of the structure to the walls of the flume are also present in all test cases. These scour patterns may have been caused by the secondary waves coming off of the structure and reaching the flume walls.

Test 4 consisted of a second bore propagating over the already scoured sand bed of Test 3. Therefore, the final local scour is slightly different than in the other cases. During the test, it was observed that sand transported by the bore from the upstream portion of the bed filled in the already present local scour hole. An additional zone of scour was however created at the front of the structure, which extended further upstream than any of the other local scour holes from the other tests.

The tests performed on the gravel bed demonstrated very similar final scour patterns than those with the sand bed. One important difference is that the scouring process was even more inhibited by the gravel over the short duration of the bore. For the largest bore depths, Tests 5, 6 and 10, the scour depth reached at the front of the structure was not as large as that reached on the sides of the structure. For the lower bore depths, Tests 7, 8 and 9, the local scour hole took the shape of two lobes on either sides of the structure. The short duration of the bore in conjunction with its lower depth and velocities in these cases may have prevented the scour initially generated at the sides to propagate up to the front of the structure. As for the deposition, in the cases with larger bore depths, the deposited gravel formed a distinct triangular shape downstream of the structure.

Test 1

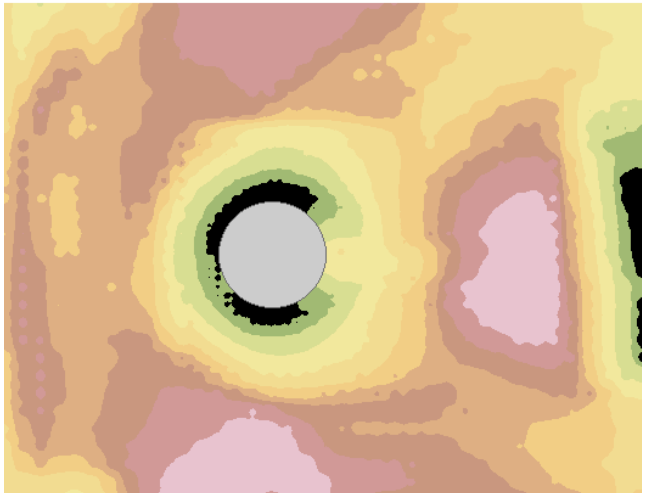

Test 2

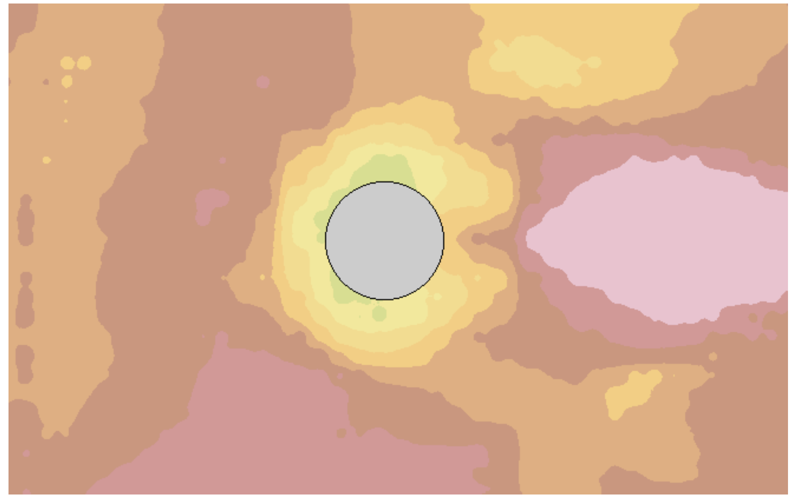

Test 3

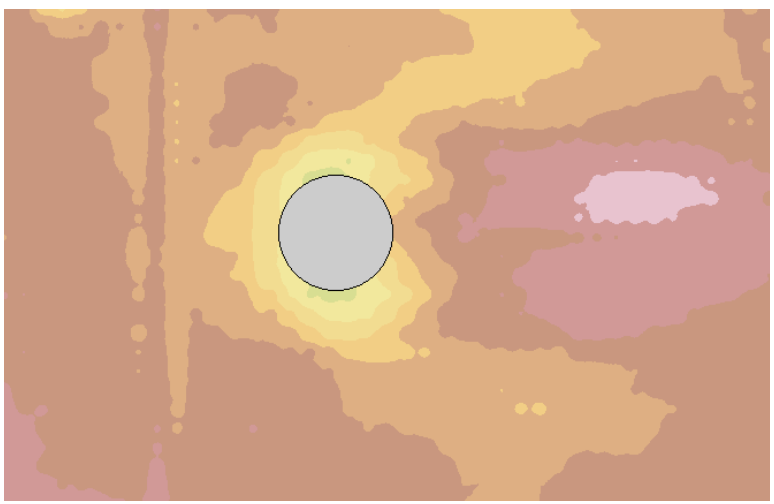

Test 4

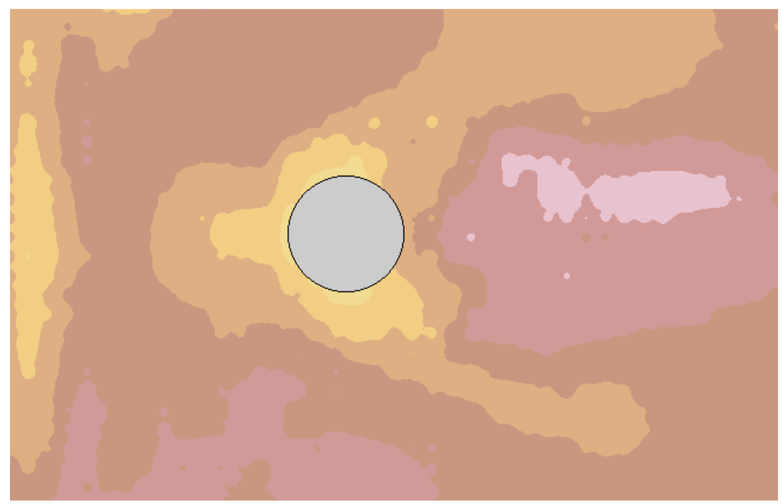

Test 5

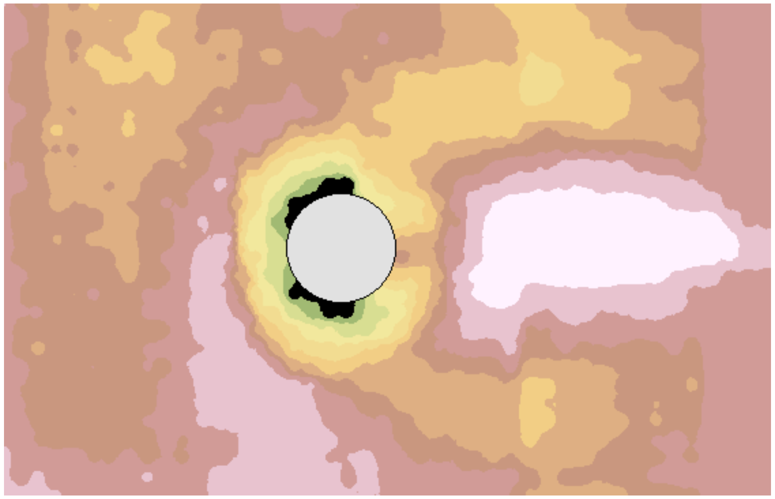

Test 6

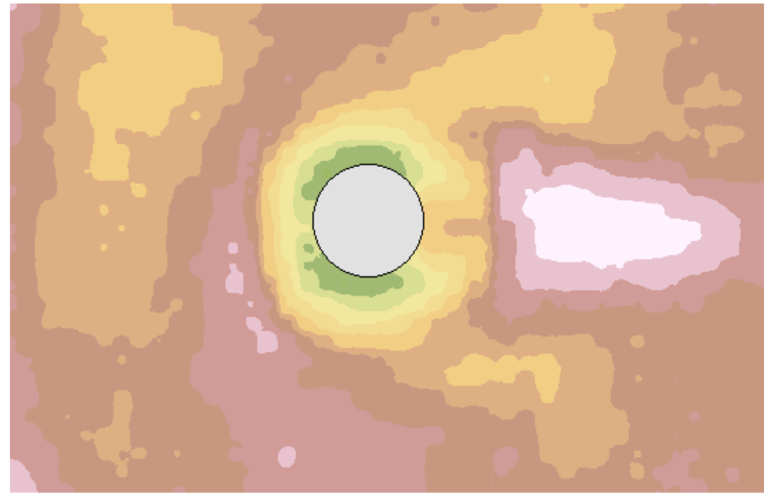

Test 7

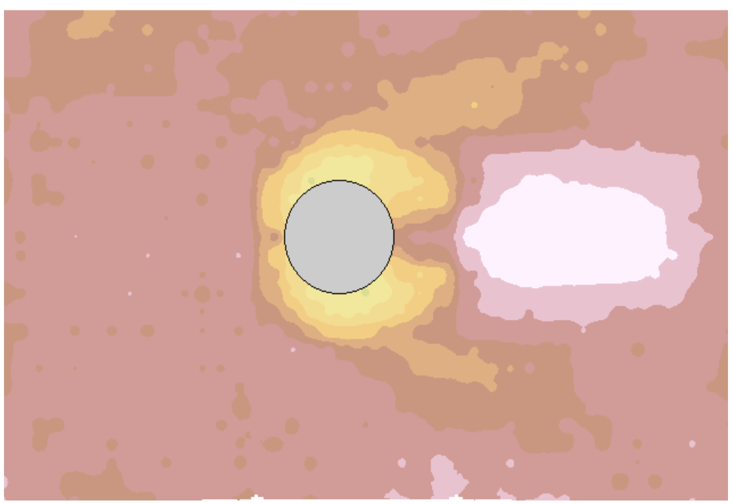

Test 8

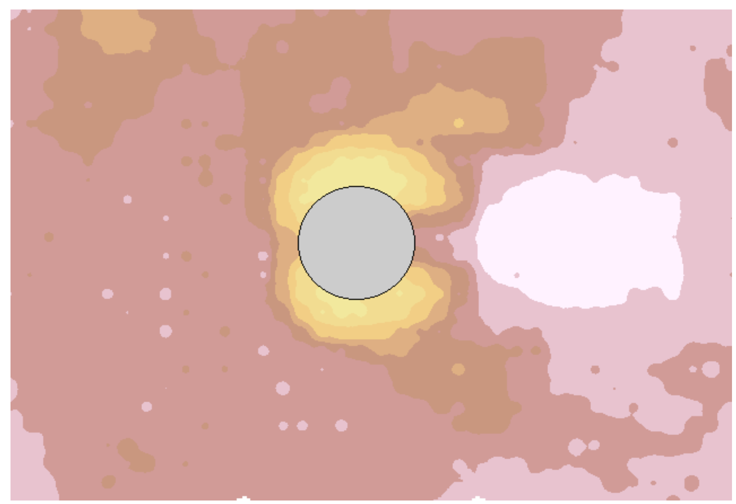

Test 9

Test 10

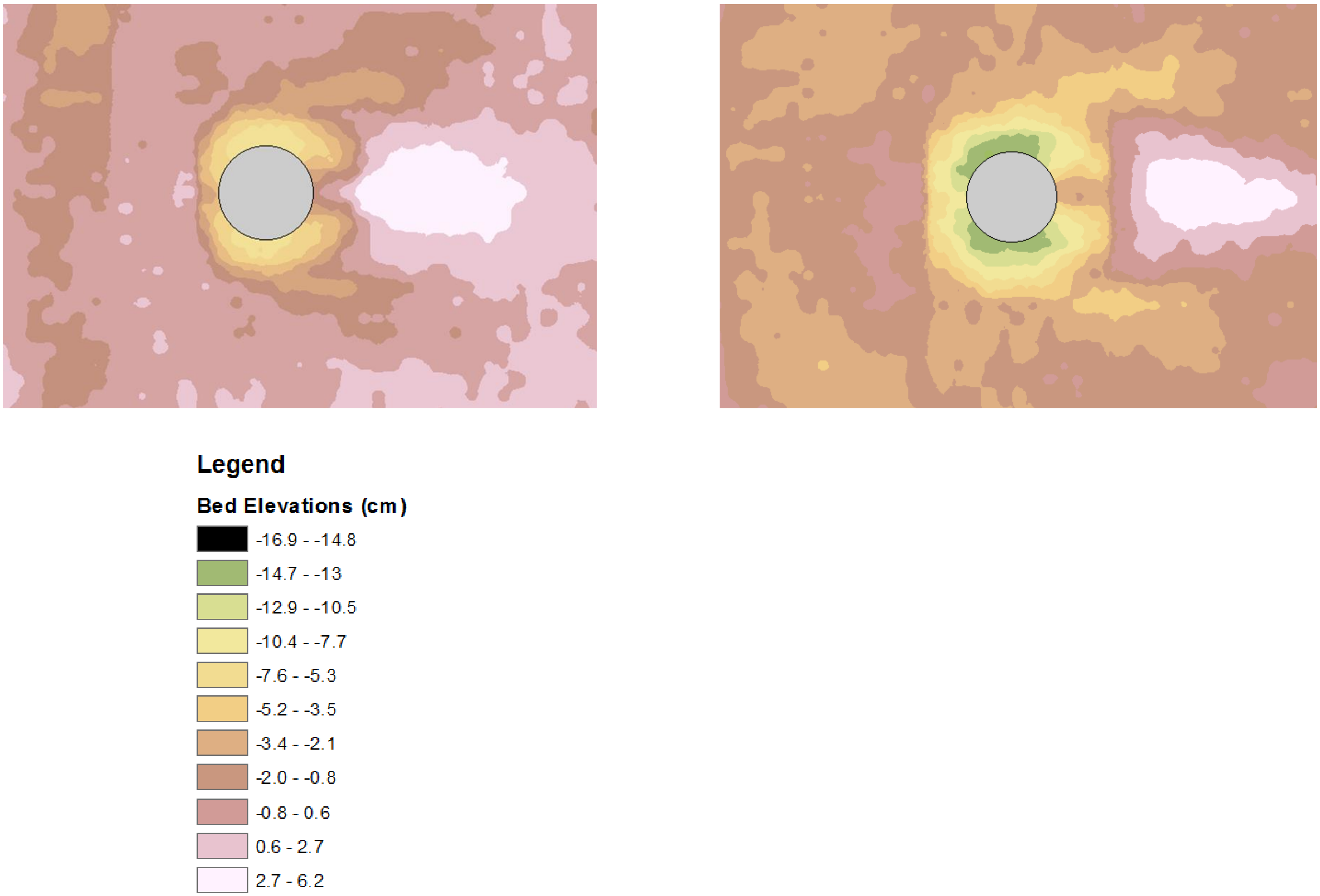

Figure 48: Final Scour Elevations

From these scour plots; the maximum scour depth for each test was determined, as shown in the table below. The ratio of the scour hole depth to the diameter of the structure is also given. These ratios vary between 32% and 71%, being as expected higher for the tests with the sand bed.

Table 5: Local Scour Hole Depth and Width Results

Test	Maximum Bore Depth (cm)	Maximum Scour Depth (cm)	Maximum Scour Depth/Structure Diameter
1	30.1	21.25	0.71
2	10.5	13.74	0.46
3	7.1	12.81	0.43
5	26.9	16.96	0.57
6	24.1	16.1	0.54
7	15.9	11.04	0.37
8	15.4	10.47	0.35
9	14.4	9.64	0.32
10	21.5	15.83	0.53

The relationship between the maximum scour depth and the maximum bore depth is plotted in Figure 49. For the sand bed, there appears to be an approximately linear relationship between the scour depth and the bore depth, but the evidence for this is weak due to the small number of points and the larger spread between the results. For the gravel tests, the observed scour depths lie within a reasonably tight range of 63% to 74% of the corresponding bore height (see Section 6.4.3), and a distinct relationship between the bore depth and scour depth can be seen. The rate at which the scour depth increases differs between the tests with higher bore depths and those with lower bore depths. For the tests with lower bore depths, Tests 7, 8 and 9, the scour depth increases proportionately with the increase in bore depth. For the tests with higher bore depths, Tests 5, 6 and 10, the scour depth increases at a much lower rate with the increase in bore depth.

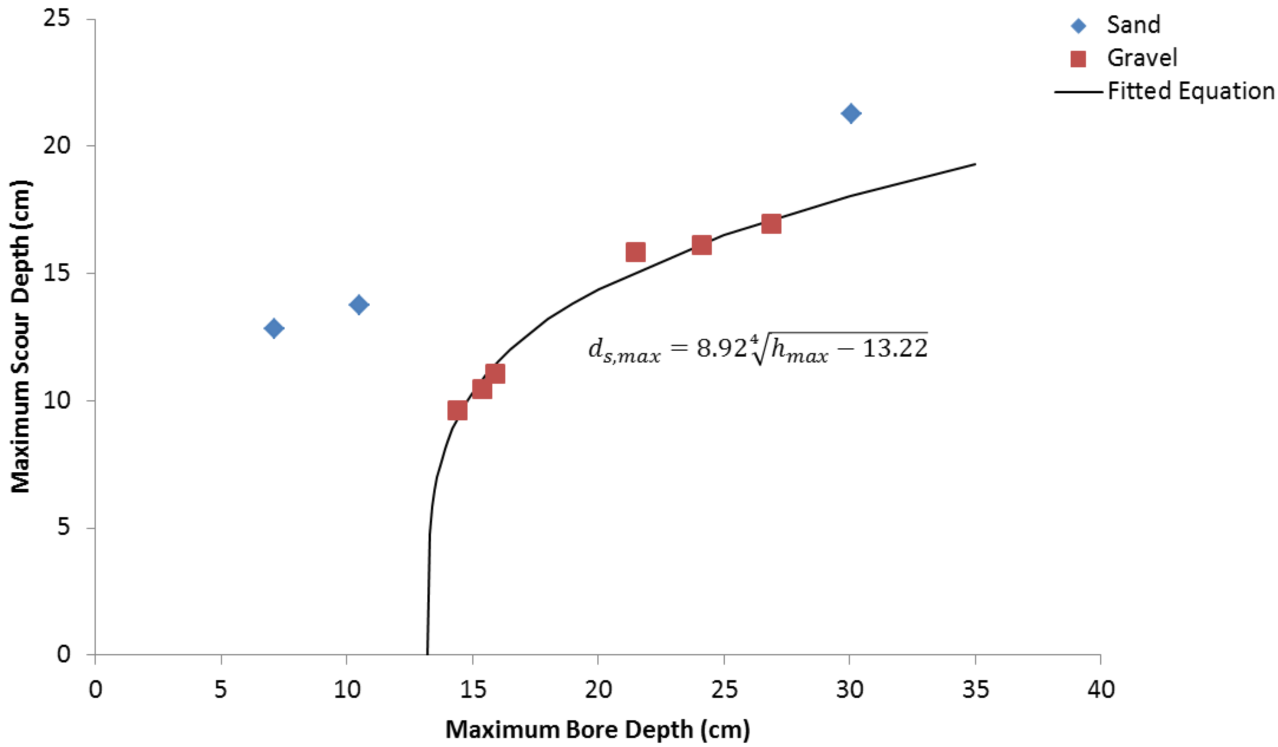

Figure 49: Relationship between Maximum Bore Depth and Maximum Scour Depth

This change in rate of scour can be well approximated using a power function. The best fitting curve is outlined in the graph above. The FEMA P646 equation defines the bore velocity as a function of the square root of the bore depth. This would suggest that scour depth is a ¼ power function of bore depth. As the results show, the changing rate of scour as the depth of the bore increases is well represented by the ¼ power function. Thus, it becomes evident that the rate of increase of scour is highly dependent on the rate of increase of bore velocity. Additional tests would be required to verify if the relationship observed between the maximum scour depth and maximum bore depth is in fact related to the relationship proposed by FEMA between the bore depth and bore velocity.

6. Comparison of Experimental Results

6.4.1 Research of Tonkin and Nakamura

In order to better appreciate the significance of the results of the present study, a comparison of these with the results of other similar studies is provided in this chapter. As described in the literature review, the experimental models of Tonkin et al. (2003) and Nakamura et al. (2008) are at present the most comparable studies to the one at hand. The similarities between all three studies are mainly present in the observed local scouring process. The process described in Section 5.2 suggests that the key scouring mechanisms are the accelerated local flows on either sides of the structure and the horseshoe vortex formed at the front of the structure. The images captured by Tonkin et al. (2003) from within their circular structure coincided with certain aspects of the scouring process observed in the current study, although the former study relied on relatively short period broken waves, unlike the longer duration bores. It was the scouring process for the uprush portion of their tests that was most comparable. The formation of the horseshoe vortex was observed to be the result of the breaking of the solitary wave very near to the front of the structure. For the tests in the present study, the bore was already fully broken as it moved toward the structure, yet the scour evidence indicated the presence of a similar vortex at the front of the structure. Tonkin et al. (2003) were able to determine that the scouring at the sides of the structure caused the sand particles to become suspended in the flow and transported much further downstream of the structure; whereas the gravel particles moved as bedload and were deposited closer to the back of the structure. Although the sediment transport was not captured or analysed in the present study, the final scour plots indicate that a similar process occurred. There was a distinct area of downstream deposition in the case of tests with a gravel bed, but in the tests with sand, the deposition occurred at a much lower magnitude. Thus, it is probable that the sand particles were transported past the sediment bed.

Nakamura et al. (2008) observed a very similar scouring process around their square structure, with concentrated flow causing significant scouring at the sides of the structure and sediment being transported downstream. Importantly, they determined that settlement of the sediment in and near the local scour hole caused the final scour depths to be 75% to 90% that of the maximum scour depths. Because Nakamura et al. (2008) conducted their tests using both solitary and long waves, they were able to assess the effects of flow duration on scour. They observed that the solitary waves were unable to scour the bed at the back of the structure, but that the long waves had a duration long enough to produce scour at the back of the structure for the sand bed. In the present study, scour was observed at the back of the structure, but not at the same magnitude as that at the front of the structure. The duration of the bores was similar to that of the long waves. Therefore, other factors such as the flow depth, flow velocity and structure geometry may have influenced the presence of scour at the back of the structure. Nakamura et al. (2008) did however conclude that for the same overtopping heights, or flow depths, the scour depths induced by long waves were always higher than those induced by solitary waves. The figure below shows their results, as well as those of the research at hand, in non-dimensionalized values of bore depth and maximum scour depth. The comparison clearly shows that the scour depths reached by the solitary waves, represented by the white squares, was consistently lower that those reached by long waves or bores. Additionally the bores, due to their longer flow duration, were able to scour the bed more than the long waves.

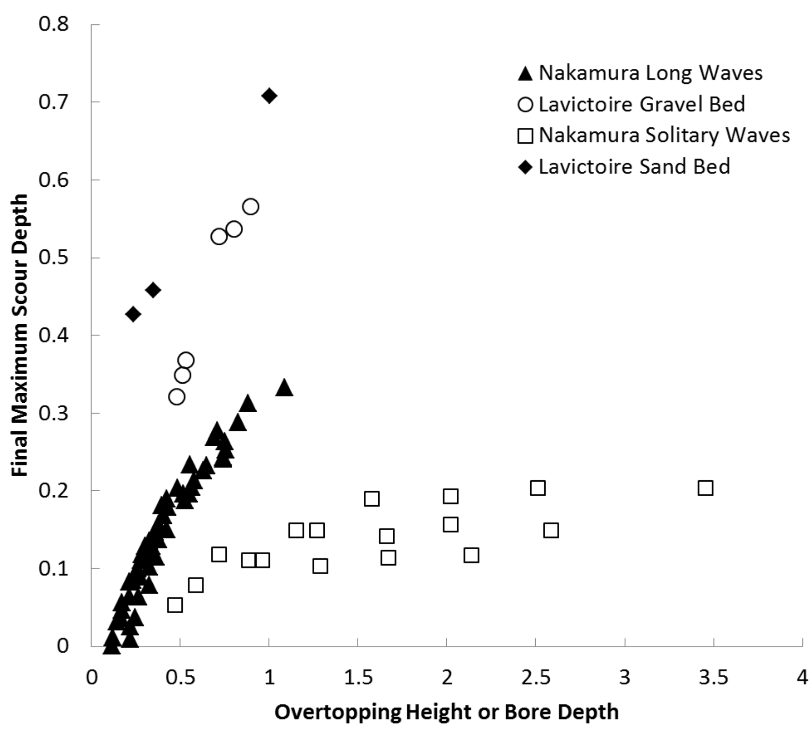

Figure 50: Relationship between Final Scour Depth and Overtopping Height (Nakamura et al., 2008)

6.4.2 Field Observations

In this section, the results of the scour test will be compared to observations and assessments of field conditions. In the proposed Tsunami Loads and Effects Chapter of ASCE7, images taken in the field by Ian Robertson and Mathew Francis of the aftermath of the Tohoku tsunami are included. They provide quantification of the tsunami wave characteristics, as well as a number of examples of local scour caused by the tsunami.

The 2011 Tohoku Tsunami was one of the first tsunamis to be extensively televised as the waves approached the Japanese coastline and propagated inland. The availability of this type of video footage allowed researchers to analyse the tsunami wave at various locations and under a number of conditions. Robertson conducted an extensive analysis of the wave propagation captured by these videos, which is included in the Tsunami Loads and Effect Chapter. With many videos showing the wave moving past landmarks or through streets, he was able to find the location of each video using Google Earth. By tracking the propagation of the wave in the video and determining the distances travelled, he could provide estimates of the propagation velocity of the tsunami wave. Table 6 below shows four examples of wave tracking by Robertson (ASCE, 2010). The first two examples were characterized as bores and the final two as surges. The locations and surfaces over which the wave travelled are different for each case. Thus, the velocities estimated range from 3.75 to 9.78 m/s. Unfortunately, these estimates are not easily comparable to the results of the present study.

For the case of the tsunami wave travelling up the Natori River in the form of a river bore, Robertson (ASCE, 2010) was able to determine the depth of the bore. Because of the concrete banks of this river visible in the video footage, the maximum height reached by the bore was known and later measured while on site. Figure 50 shows an image of the Natori River banks. The bore depth was estimated at 1.27 m, resulting in a Froude number of 1.95. This indicated that the tsunami wave did in fact become a fully broken bore as it travelled inland. Although the Froude number of this field result is much higher than those achieved by the bores in the experimental model, both cases have Froude numbers higher than the lower limit for a fully broken bore. The bore characteristics were therefore adequately captured in the experimental tests.

Figure 51: Concrete Sloped Banks of the Natori River (Robertson, ASCE 2010)

Table 6: 2011 Tohoku Tsunami Wave Tracking and Velocities

<table>
<tr><th>Wave Type</th><th>Estimated Velocity (m/s)</th><th>Location</th><th>Surface Type</th><th>Image</th></tr>
<tr><td>River Bore</td><td>6.89</td><td>Natori River</td><td>River</td><td>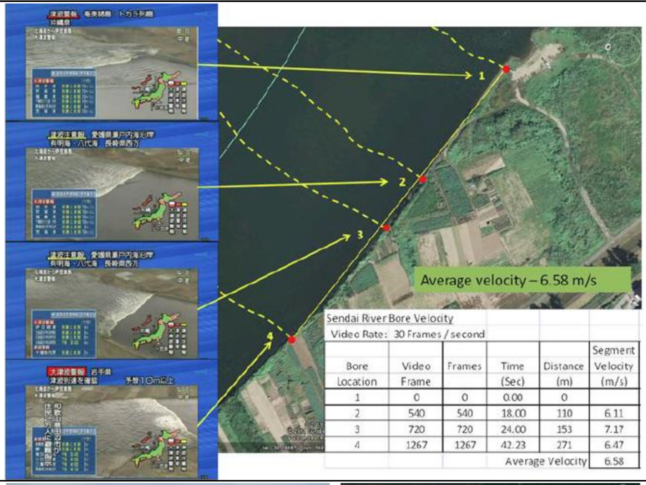
</td></tr>
<tr><td>Harbor Bore</td><td>9.78</td><td>Noda Tamagawa</td><td>Harbour water</td><td>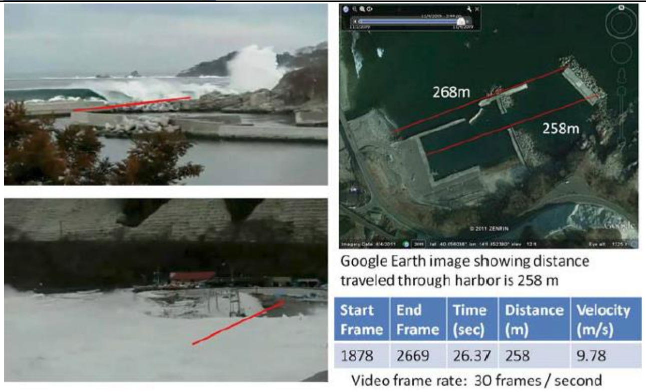
</td></tr>
</table>

Surge	6.34	Sendai	Farmland	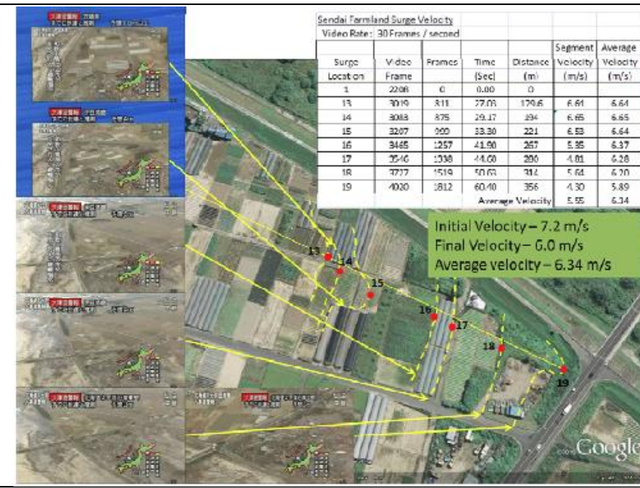
Surge	3.75	Kamaishi	Street	

Field observations of scour were collected during the field surveys of the Tohoku tsunami conducted by Francis and Robertson (ASCE, 2010). Different types of scour were observed, including scour of beaches, at sea walls, of pavement and roads, as well as local scour at building corners and other structures. Table 7 provides examples of local scour observations which include the flow depth, scour depth and soil type for each case. The influence of a number of factors, including location, wave velocity and depth, soil type and structure shape is evident when considering the wide range of scour depths recorded. As with the estimated tsunami wave velocities, most of these scour depths are not easily comparable with the results of the present study.

There is however one observation of local scour that offers an excellent comparison to the experimental results. The viaduct pier in Miyako City exhibited a textbook local scour hole. The viaduct spans the Miyako River inlet and although the bridge itself did not sustained any structural damage caused by the tsunami wave, the clay soil surrounding its piers was heavily scoured. A flow depth of 6 m was estimated for this location and the scour depth measured at 4.2 m. Unfortunately, the diameter of the pier was not recorded, however the flow depth to scour depth ratio will be analysed in the next chapter.

Table 7: 2011 Tohoku Tsunami Local Scour Field Observations

Site Features	Flow Depth (m)	Scour Depth (m)	Location	Soil Type	Image
Railroad, bridge	6	1	Yagi Port	Sand and fill	
Bridge, viaduct pier	6	4.2	Miyako City	Sand and clay	

Building, corner footing	unknown	1.4	Tarou	Sand and fill	
Building, corner foundation	17	3	Kamaishi City	Gravel and fill	
Palm tree	5.5	none	Choshi Marina	Sand	

6.4.3 Tsunami Scour Design Prescriptions

The results of both the experimental tests and the field observations can also be compared to the design guidelines for structures in areas at risk of tsunamis. As was introduced in the literature review, current design guidelines rely on the scour depth ratios proposed by Dames and Moore (1980) in the table below. The ratios are taken as the scour depth divided by the flow depth and values are given for structures located close to or far from the shoreline with different soil types. There are no ratios provided for foundations embedded in gravel.

Table 8: Design Guidelines for Scour Depth

Table 7-1 Approximate Scour Depth as a Percentage of Flow Depth, *d* (Dames and Moore, 1980)

Soil Type	*Scour depth (% of d) (Shoreline Distance < 300 feet)*	*Scour depth (% of d) (Shoreline Distance > 300 feet)*
Loose sand	80	60
Dense sand	50	35
Soft silt	50	25
Stiff silt	25	15
Soft clay	25	15
Stiff clay	10	5

Table 9: Experimental Scour to Flow Depth Ratios

Test	Sediment Type	Maximum Bore Depth (cm)	Maximum Scour Depth (cm)	Scour/Flow Depth Ratio
1	Sand	30.1	21.25	71
2	Sand	10.5	13.74	131
3	Sand	7.1	12.81	180
5	Gravel	26.9	16.96	63
6	Gravel	24.1	16.1	67
7	Gravel	15.9	11.04	69
8	Gravel	15.4	10.47	68
9	Gravel	14.4	9.64	67
10	Gravel	21.5	15.83	74
Viaduct Pier	Sand and Clay	600	420	70

The same ratios were calculated for the experimental tests and for the field observation at the viaduct pier in Miyako City, provided in Table 9. When comparing the results to the ratios suggested by Dames and Moore (1980) for structures located far from the shoreline, the experimental ratios are all much higher. For a sand bed, the guidelines suggest designing for ratios of 35 to 60%. The ratios of the experimental tests conducted with a loose sand bed ranged from 71 to 180%. The ratio for Test 1 was not calculated based on the maximum scour depth because the local scour hole reach the bottom of the sediment bed. Even so, the experimental ratios for sand surpass the proposed ratios by almost 100%. As for the experimental tests carried out on a gravel bed, the ratios ranged from 63 to 74%. Although gravel is not included in the Dames and Moore (1980) table, if comparing them to the ratios for clay, the guidelines are underestimating the potential scour by more than 50%. Finally, if the case of the scour observed at the viaduct pier is compared, the scour ratio of 70% for this case should be comparable to a ratio of 35% in the guidelines for dense sand. Once again, the scour to flow depth ratio is significantly underestimated for the potential, and in this case actual, local scour induced by a tsunami wave.

7. Conclusions and Recommendations

6.1 Conclusions

An experimental investigation conducted on a physical model was undertaken in order to investigate the local scour induced by hydraulic bores. A series of fully broken bores was successfully simulated in laboratory using the technique of an impounded volume of water suddenly released by a swinging gate. Measures were taken to ensure full separation of the gate from the water and that the bores propagated evenly. Measurements of the bore depth time history validated the vertical initial profile of the bores, with maximum depths reached within 10 seconds. Analysis of the high speed video camera footage produced three types of velocity measurements, notably average bore front velocities, instantaneous bore front velocities and the sustained flow velocities. Finally, the interpolation of the final sediment bed elevations revealed the characteristics of the local scour hole and other scour and deposition patterns.

In this study, several relationships between the different bore and scour characteristics were determined. A linear relationship between the maximum bore depth and the reservoir water depth was identified. This increase in bore depth led to an increase in flow acceleration and implicitly, of the flow velocity. Furthermore, the relationship between the maximum scour depth and the maximum bore depth indicated that the scour was highly dependent on the bore velocity for the tests conducted with gravel. Finally, there was also a relationship between the reservoir water depth and the sustained flow deceleration.

The primary objective of this study was achieved, in that the video footage and final scour plots of the experimental tests revealed that bores do produce a unique scouring process. The following points highlight the main conclusions of this study:

- The relationship between the bore depths and bore front velocities was very similar to the equation proposed by FEMA P646 (2012). In this experimental program, the average bore front velocities ranged from 1.16 to 2.14 m/s and all bores were fully broken upon entering the sediment bed test section, having computed Froude numbers surpassing 1.3.

- The short duration and very turbulent nature of the bores induced a rapid scouring process. Significant scour depths were reached, yet evidence that the scouring process was incomplete was observed. For large bore depths and for the sand bed, the local scour holes were circular in shape. For low bore depths with a gravel bed, the local scour holes formed two lobes on either side of the structure. This incomplete scour hole formation was attributed to the relatively short duration of the bore. The importance of the effect of the bore duration on the scouring process was also underlined in the research by Nakamura et al. (2008).

- Sand particles were entrained and displaced away from the structure by the bore, whereas gravel particles moved as bedload and were deposited downstream of the structure. This difference in sediment transport was also observed by Tonkin et al. (2003).

- Final scour depth to structure diameter ratios ranged from 32 to 71%, with scour depths reaching the bottom of the sediment bed in some cases. Ratios of scour depth to flow depth ranged from 63 to 180%. The ratios suggested in current design guidelines significantly underestimate the potential scour depths induced by bores.

6.2 Recommendations for Future Work

The observations made in the field investigations revealed that characteristics of tsunami waves, such as their propagation velocity and their scouring potential, vary greatly. Because of this important variability, studies such as this one provide useful, although very limited, analysis and understanding of these complex natural phenomena. Thus, the potential for future work in this field of study is endless. Here are some recommendations that pertain specifically to the results of the current experimental study:

- Further investigation into the vortex formation when a bore impacts a structure. Evidence that the turbulent characteristics of the flow surrounding the structure are different for large bore depths than for small bore depths was observed in this study. Additional analysis of these flow patterns could shed light on the scouring process induced by the bores.

- Investigation of the effect of bore propagation velocity on maximum scour depth. Two distinct relationships between bore velocity and scour depth were observed in this study. A larger sample of tests is required to better define this relationship and evaluate the dependency of scour depth on bore velocity.

- Further investigation into the sediment transport induced by bores for various types of sediment. Although no analysis of sediment transport was undertaken in this study, evidence of differences in the transport of sand versus gravel sediment was observed.

Finally, because this research was conducted strictly on the local scour caused by bores, it is necessary to combine it with research related to the other effects of bores on structures, such as the one by Al-Faesly et al. (2012) on the impact forces of tsunami waves on structures. Results of these types of physical models can then be used to validate numerical models, which provide an optimal method of simulating and analysing the interaction between tsunamis and structures.

8. References

Adduce, C., & Sciortino, G. (2006). Scour Due to a Horizontal Turbulent Jet: Numerical and Experimental Investigation. *Journal of Hydraulic Research, 44*(5), 663-673.

Al-Feasly, T., Palermo, D., Nistor, I., & Cornett, A. (2012). Experimental Modeling of Extreme Hydrodynamic Forces on Structural Models. *Internaltional Journal of Protective Structures, 3*(4), 477-505.

Arnason, H. (2005). *Interactions between an Incident Bore and a Free-Standing Coastal Structure.* University of Washington, Department of Civil and Environmental Engineering.

ASCE, 2010. Minimum Design Loads for Buildings and Other Structures, *ASCE/SEI Standard 7-10, American Society of Civil Engineers, Reston, Virginia, USA.*

Brown, R., & Chanson, H. (2012). Suspended Sediment Properties and Suspended Sediment Flux Estimates in an Inundated Urban Environment During a Major Flood Event. *Water Resources Research, 48*, 1-15.

Chadwick, A., Morfett, J., & Borthwick, M. (2004). *Hydraulics in Civil and Environmental Engineering.* Abingdon: Spon Press.

Chanson, H. (2004). *The Hydraulics of Open Channel Flow.* London: Elsevier Butterworth-Heinemann.

Chanson, H. (2006). Tsunami Surges on Dry Coastal Plains: Application of Dam Break Wave Equations. *Coastal Engineering Journal, 48*(4), 355-370.

Chanson, H., Aoki, S., & Maruyama, M. (2003). An Experimental Study of Tsunami Runup on Dry and Wet Horizontal Coastlines. *Science of Tsunami Hazards, 20*(5), 278-293.

Chanson, H., Reungoat, D., Simon, B., & Lubin, P. (2011). High-Frequency Turbulence and Suspended Sediment Concentration Measurements in the Garonne River Tidal Bore. *Estuarine, Coastal and Shelf Science, 95*, 298-306.

Chatterjee, S. S., Ghosh, S. N., & Chatterjee, M. (1994). Local Scour Due to Submerged Horizontal Jet. *Journal of Hydraulic Engineering, 120*, 973-992.

Chiew, Y.-M., & Lim, S.-Y. (1996). Local Scour by a Deeply Submerged Horizontal Circular Jet. *Journal of Hydraulic Engineering, 122*, 529-532.

Chin, C., Chiew, Y., Lim, S., & Lim, F. (1996). Jet Scour around Vertical Pile. *Journal of Waterway, Port, Coastal, and Ocean Engineering, 122*, 59-67.

Chock, G., Roberson I., Kriebel D., Francis M., Nistor, I., (2013). Tohoku Japan Tsunami of March 11, 2011 – Performance of Structures under Tsunami Loads, ASCE/SEI Report, 359 p

City and County of Honolulu Building Code (CCH) 2000. Department of Planning and Permitting of Honolulu Hawaii. *Chapter 16 Article 11. Honolulu, Hawaii.*

Crowe, C., Elger, D., Williams, B., & Roberson, J. (2009). *Engineering Fluid Mechanics.* Hoboken: Wiley.

Farhoudi, J., & Smith, K. (1985). Local Scour Profiles Downstream of Hydraulic Jump. *Journal of Hydraulic Research, 23*(4), 343-358.

Federal Emergency Management Agency. (2008). *Guidelines for Design of Structures for Vertical Evacuation from Tsunamis.* Washington D.C., USA.

Francis, M. J. (2006). *Tsunami Inundation Scour of Roadways, Bridges and Foundations.* EERI/FEMA NEHRP Professional Fellowship Report.

Jain, S., & Fischer, E. (1979). *Scour Around Circular Bridge Piers at High Froude Numbers.* The University of Iowa, Iowa Institute of Hydraulic Research. US Department of Transportation, Federal Highway Administration.

Karim, O., & Ali, K. (2000). Prediction of flow patterns in local scour holes caused by turbulent water jets. *Journal of Hydraulic Research*, *38*(4), 279-287.

Khezri, N., & Chanson, H. (2012). Inception of Bed Load Motion Beneath a Bore. *Geomorphology*(153-154), 39-47.

Koch, C., & Chanson, H. (2009). Turbulence Measurements in Positive Surges and Bores. *Journal of Hydraulic Research, 47*(1), 29-40.

Lauber, G., & Hager, W. H. (1997). Experiments to dambreak wave: Horizontal channel. *Journal of Hydraulic Research, 36*(3), 291-307.

Melville, B. W., & Coleman, S. E. (2000). *Bridge Scour.* Highlands Ranch, Colorado, USA: Water Resources Publications, LLC.

Mikami, T., Shibayama, T., Esteban, M., & Matsumaru, R. (2012). Field Survey of the 2011 Tohoku Earthquake and Tsunami in Miyagi and Fukushima Prefectures. *Coastal Engineering Journal*, *54*(1).

Moronkeji, A. (2007). Physical Modelling of Tsunami Induced Sediment Transport and Scour. *Earthquake Engineering Symposium for Young Researchers.* Seattle.

Nakamura, T., Yasuki, M., & Mizutani, N. (2008). Tsunami Scour Around a Square Structure. *Coastal Engineering Journal*, *50*(2), 206-246.

Nouri, Y., Nistor, I., Palermo, D., Cornett, A., (2010). Experimental investigation of the tsunami impact on free standing structures, C*oastal Engineering Journal*, JSCE, 52(1), 43–70.

Orendorff, B., Rennie, C., & Nistor, I. (2011). Using PTV through an embankment breach channel. *Journal of Hydro-environment Research, 5*, 277-287.

Pasternack, G. B., Ellis, C. R., & Marr, J. D. (2007). Jet and Hydraulic Jump Near-Bed Stresses Below a Horseshoe Waterfall. *Water Resources Research, 43*, 14.

Ramsden, J. D. (1993). *Tsuanmis: Forces on a Vertical Wall Caused by Long Waves, Bores, and Surges on a Dry Bed.* Pasadena, California: California Institute of Technology.

Stansby, P. K., Chegini, A., & Barnes, T. C. (1998). The initial stages of dam-break flow. *Journal of Fluid Mechanics, 374*, 407-424.

Stoker, J. (1957). *Water Waves.* New York: Interscience Publishers Inc.

Tonkin, S., Yeh, H., Fuminori, K., & Shinji, S. (2003). Tsunami scour around a cyliner. *Journal of Fluid Mechanics, 496*, 165-192.

Yoshii, T., Ikeno, M., Matsuyama, M., & Fujii, N. (2010). Pick-up Rate of Suspended Sand Due to Tsunami. *Conference on Coastal Engineering, 32.* Shanghai.

Yuksel, A., Celikoglu, Y., Cevik, E., & Yuksel, Y. (2005). Jet scour around vertical piles and pile groups. *Ocean Engineering, 32*, 349-362.

Appendix A – Wave Gauge Calibration Curves

The three wave gauges were calibrated in a separate barrel of water for depths of 0 to 70 cm. Readings were taken at 0, 20, 30, 40 and 70 cm in order to prepare the calibration curves based on the water depth and the voltage readings of the gauges. The slope and intercept of these curves was then inputted into the LabView program that was used to record and process the wave gauge readings. The figure below shows the calibration curve equations for each wave gauge.

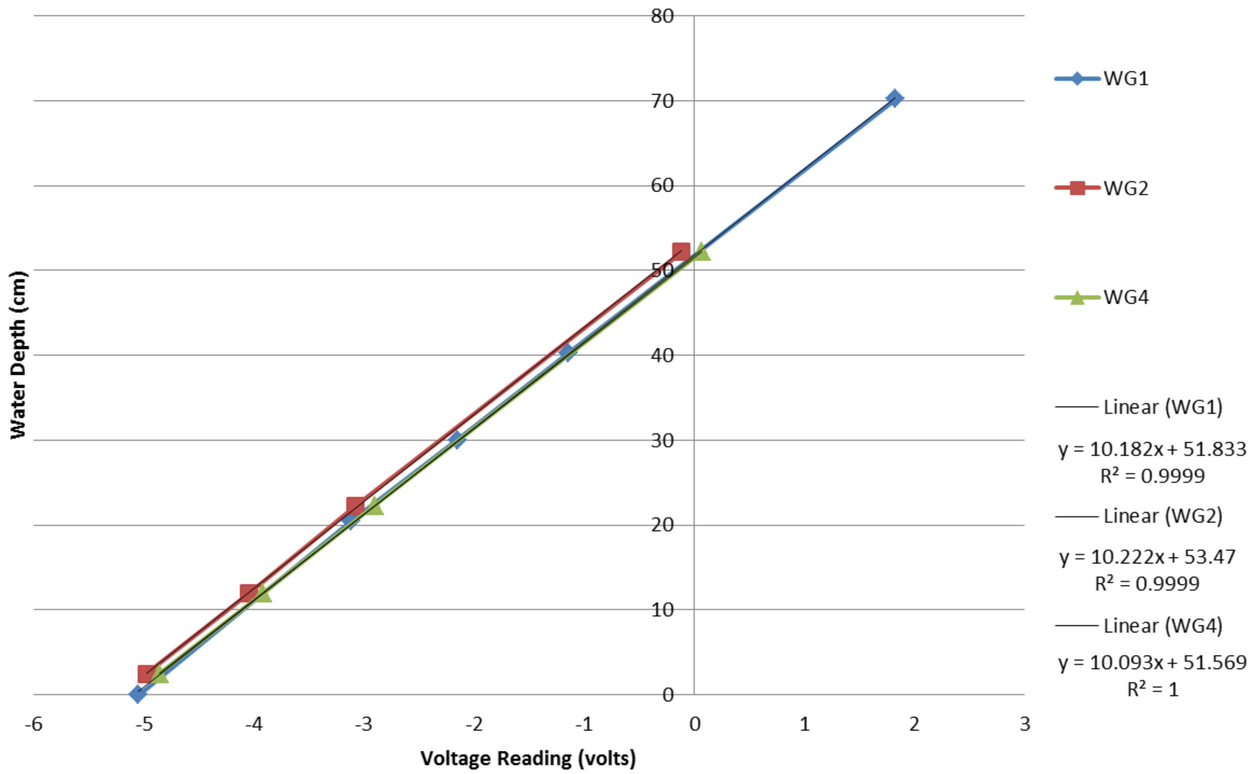

Appendix B – Time History of Water Surface Elevations

Test 1

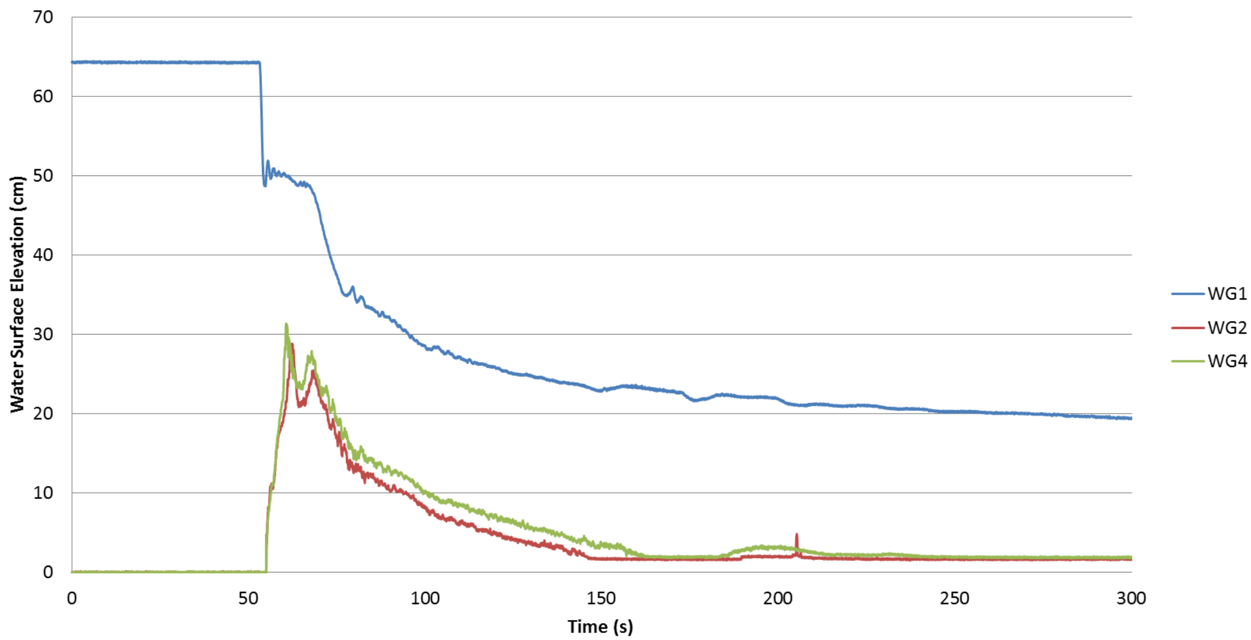

Test 2

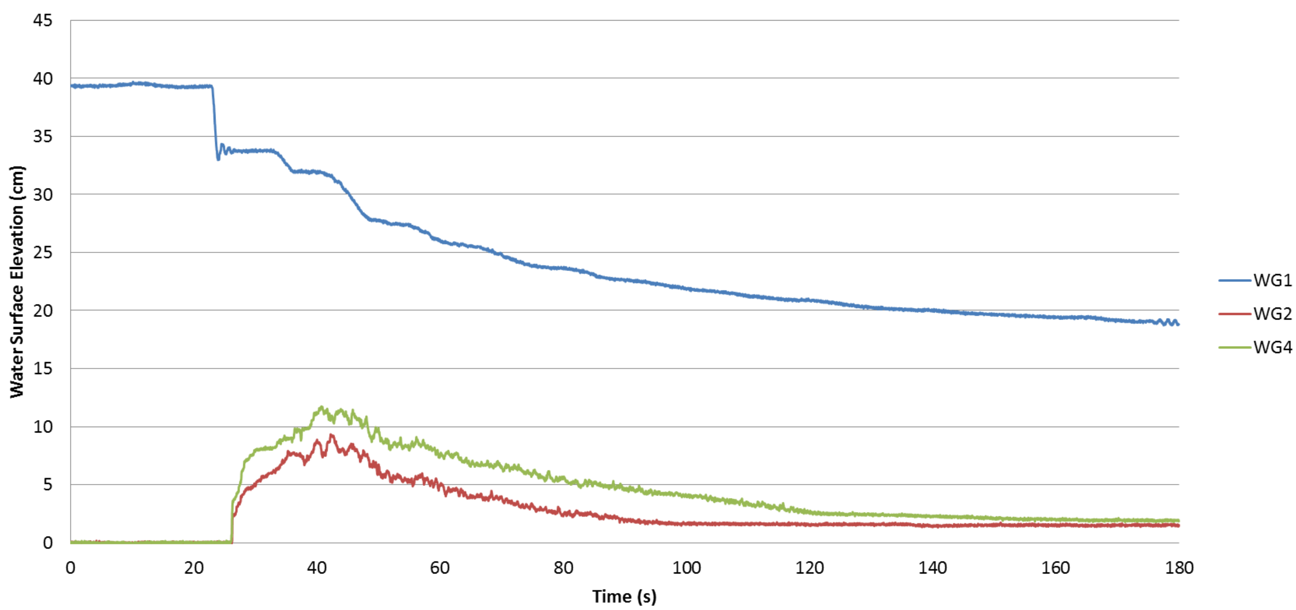

Test 3

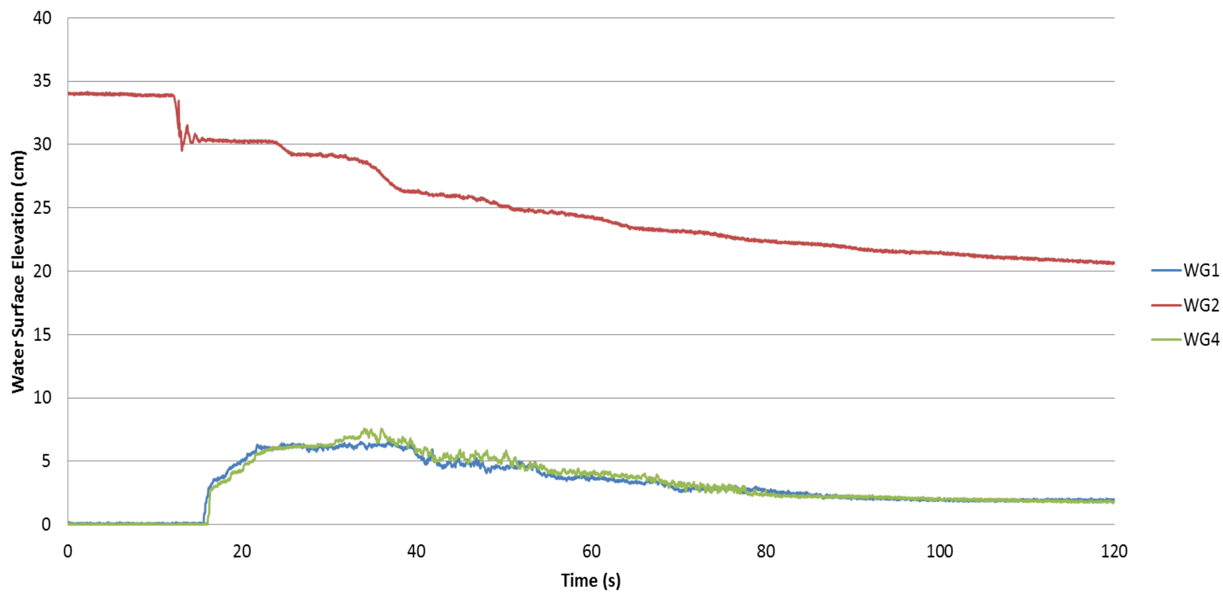

Water Surface Elevation (cm)
40
35
30
25
20
15
10
5
0
0
20
40
60
80
100
120
Time (s)
WG1
WG2
WG4

Test 4

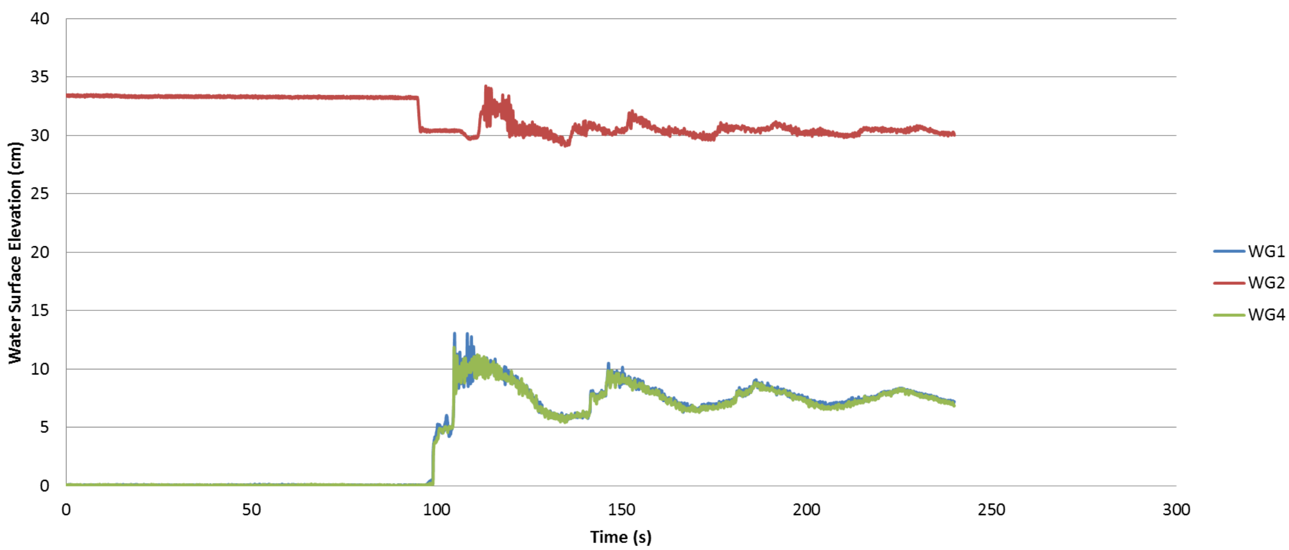

Water Surface Elevation (cm)
40
35
30
25
20
15
10
5
0
0
50
100
150
200
250
300
Time (s)
WG1
WG2
WG4

Test 5

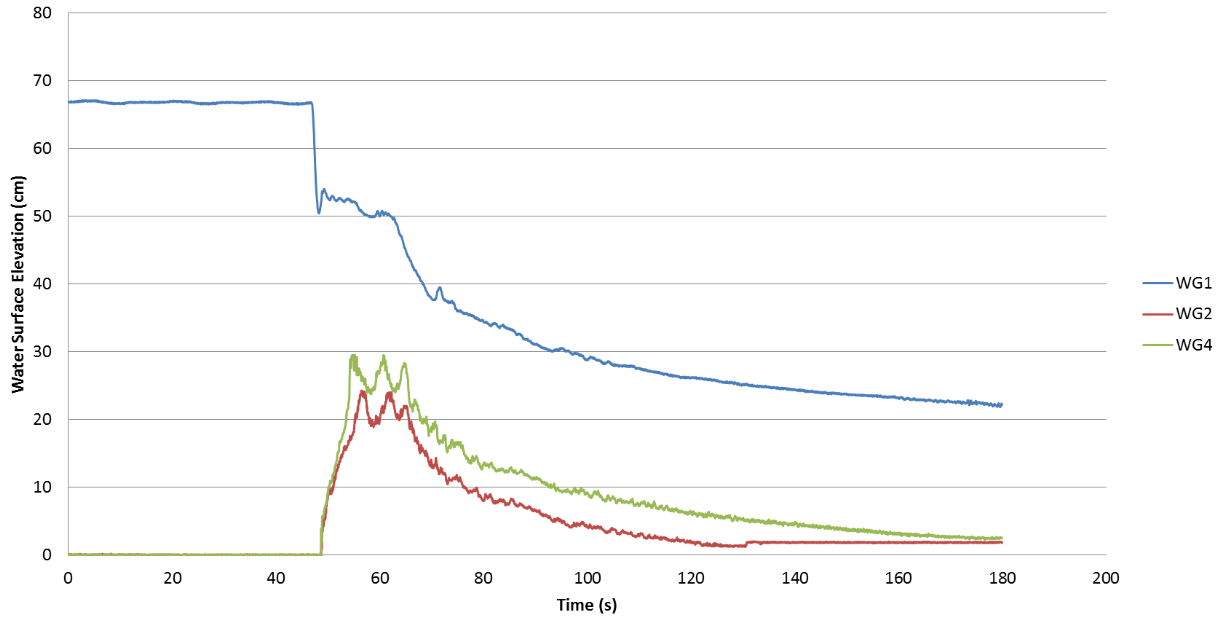

80
70
60
50
40
30
20
10
0
0
20
40
60
80
100
120
140
160
180
200
Water Surface Elevation (cm)
Time (s)
WG1
WG2
WG4

Test 6

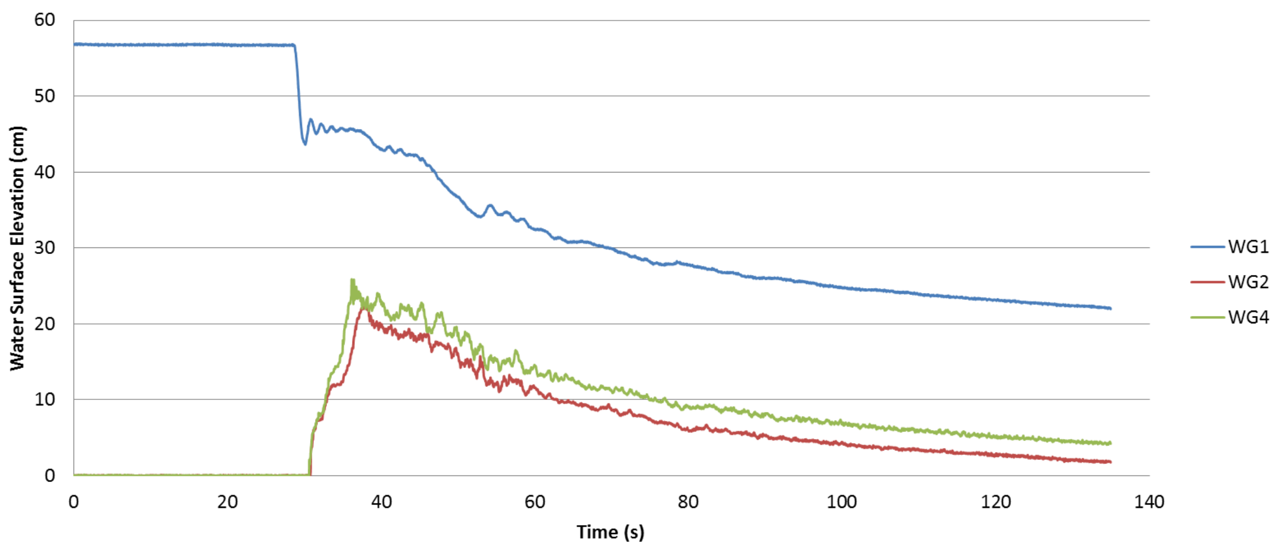

60
50
40
30
20
10
0
0
20
40
60
80
100
120
140
Water Surface Elevation (cm)
Time (s)
WG1
WG2
WG4

Test 7

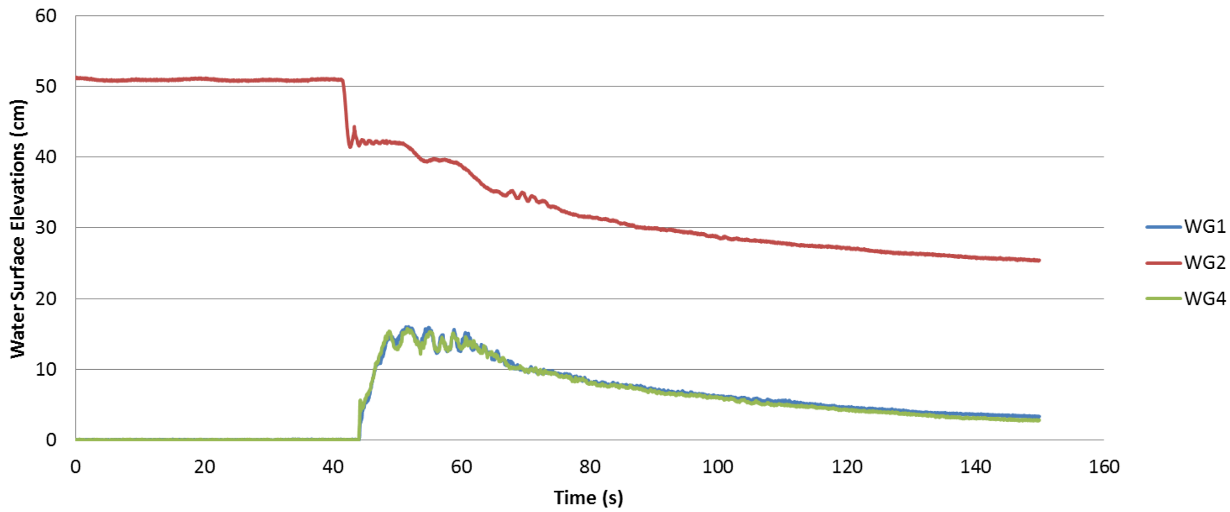
60
50
40
30
20
10
0
Water Surface Elevations (cm)
0
20
40
60
80
100
120
140
160
Time (s)
WG1
WG2
WG4

Test 8

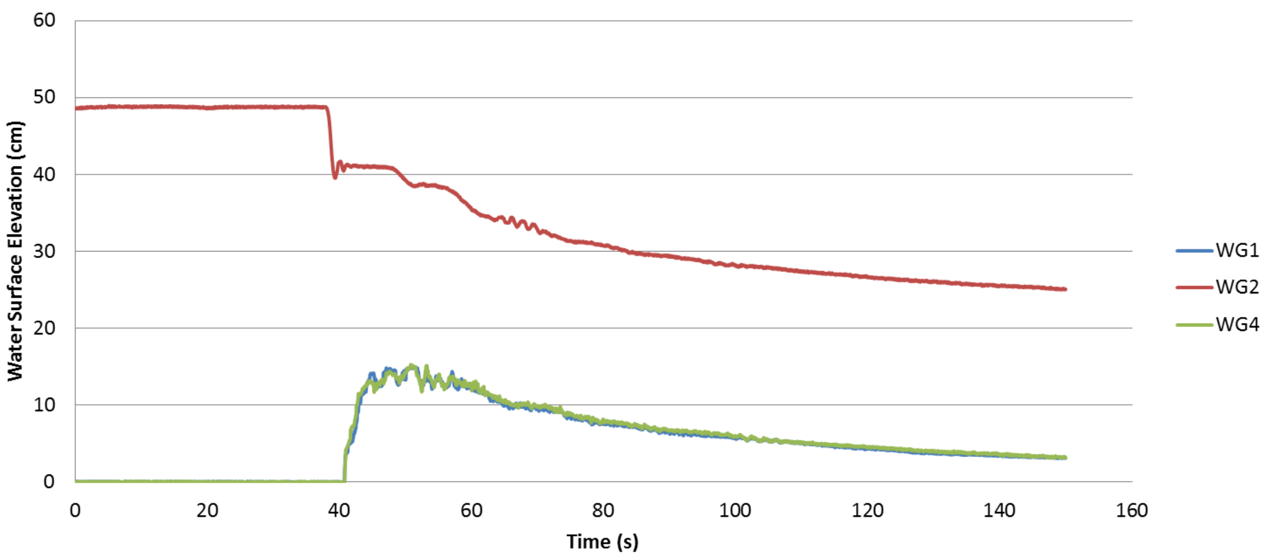
60
50
40
30
20
10
0
Water Surface Elevation (cm)
0
20
40
60
80
100
120
140
160
Time (s)
WG1
WG2
WG4

Test 9

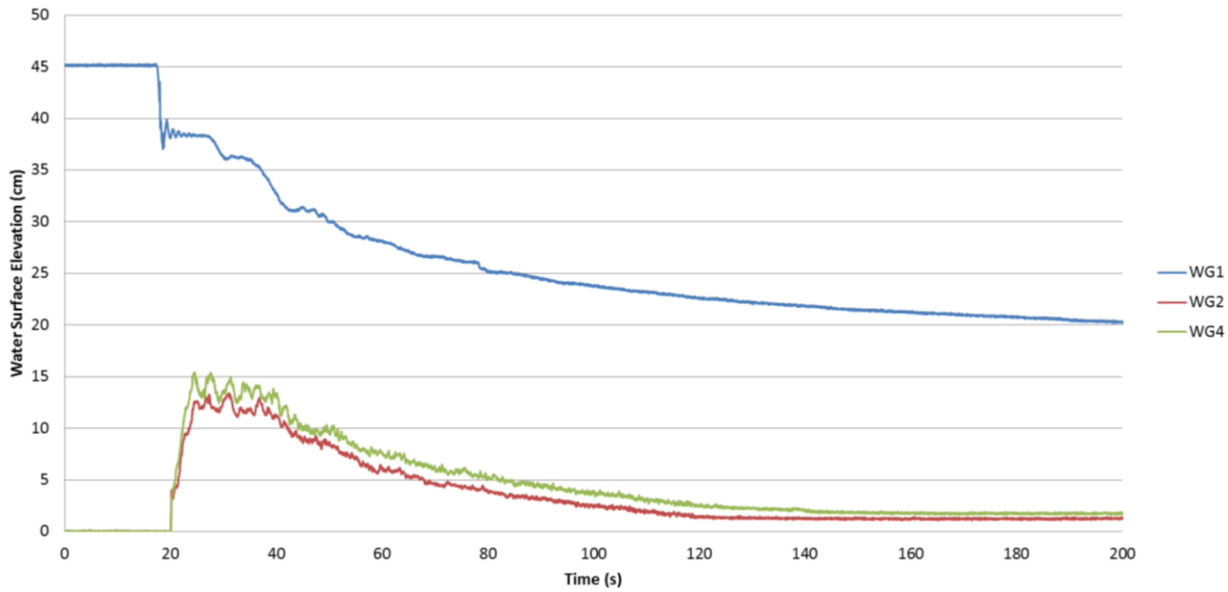

Test 10

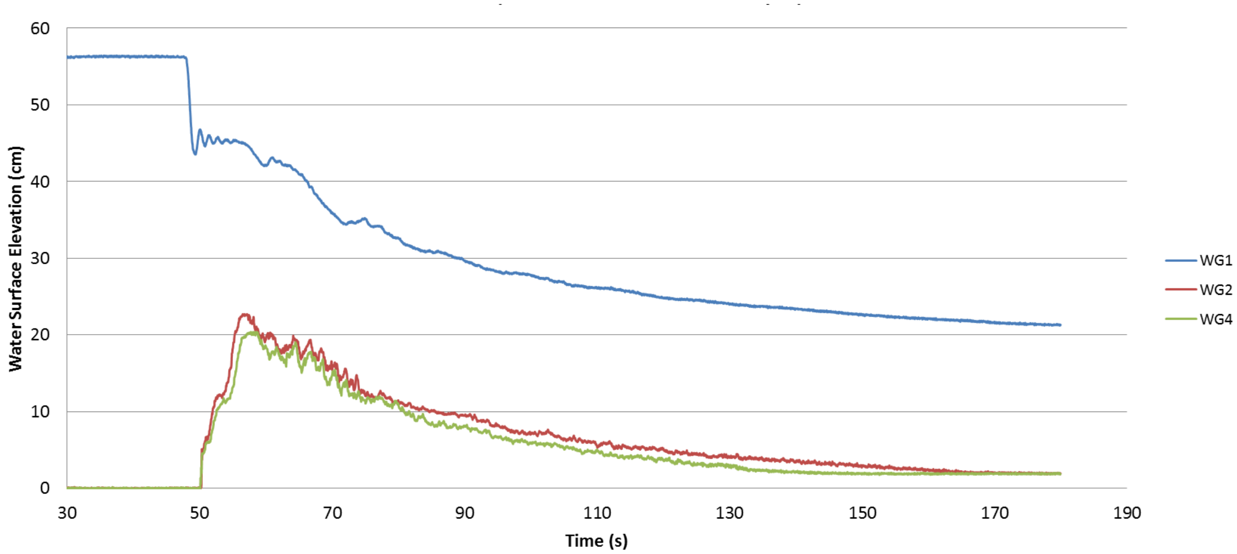

Appendix C – Streamwise Sediment Bed Cross-Sections

Test 1

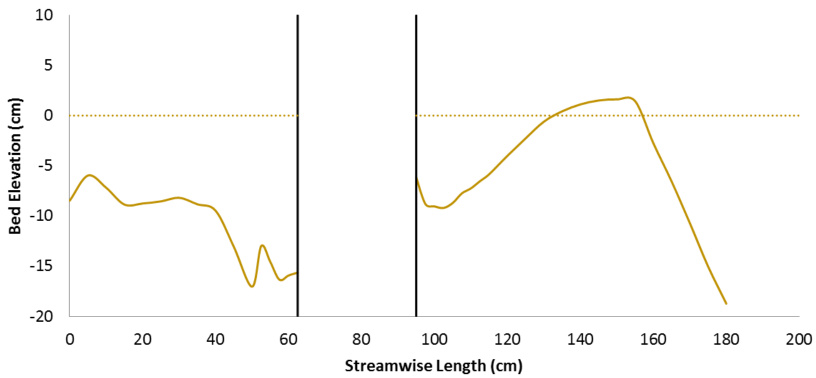

Test 2

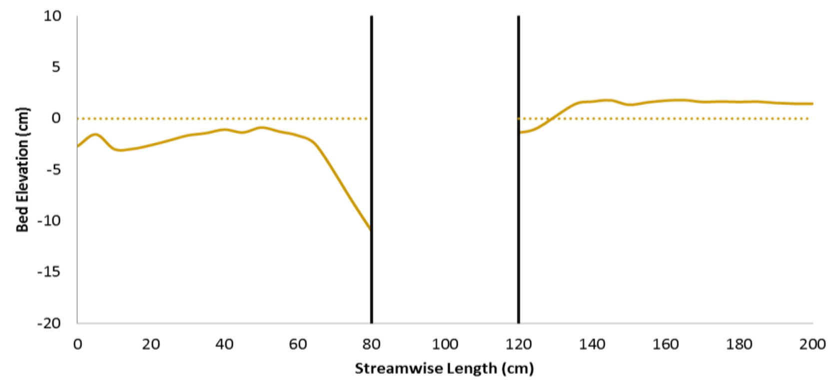

Test 3

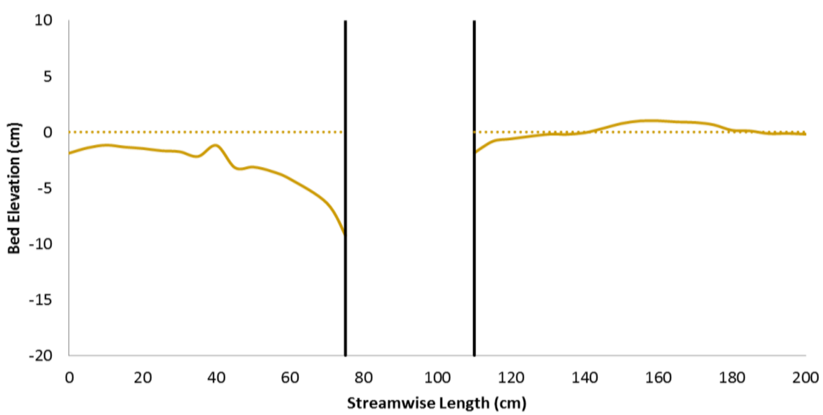

Test 4

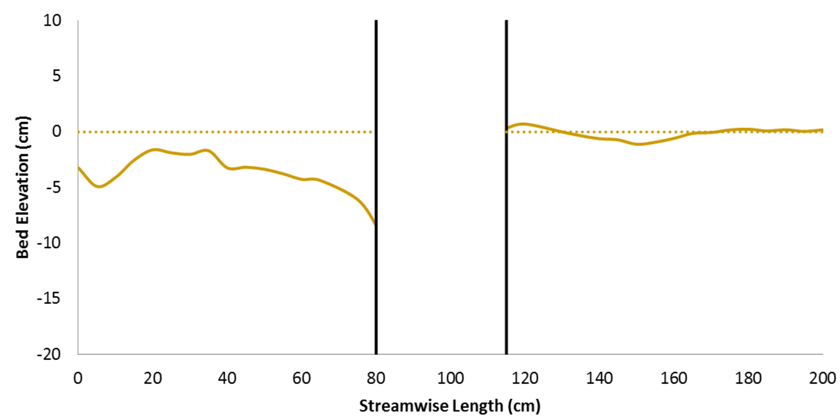

Test 5

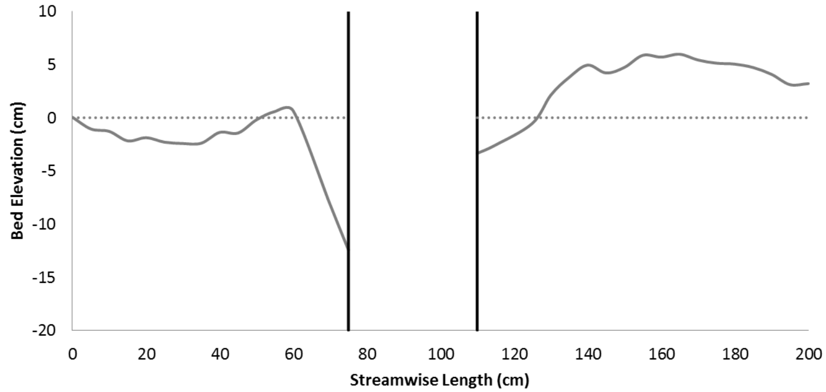

Test 6

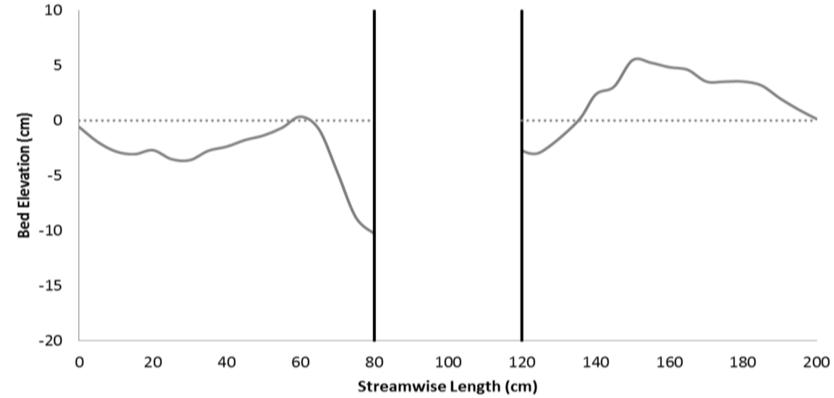

Test 7

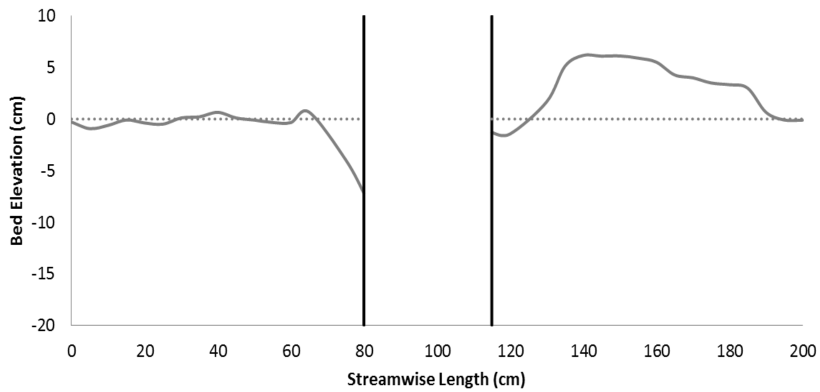

Test 8

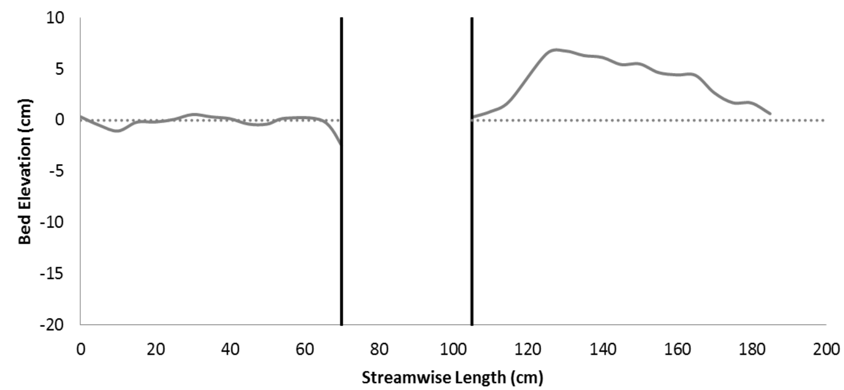

Test 9

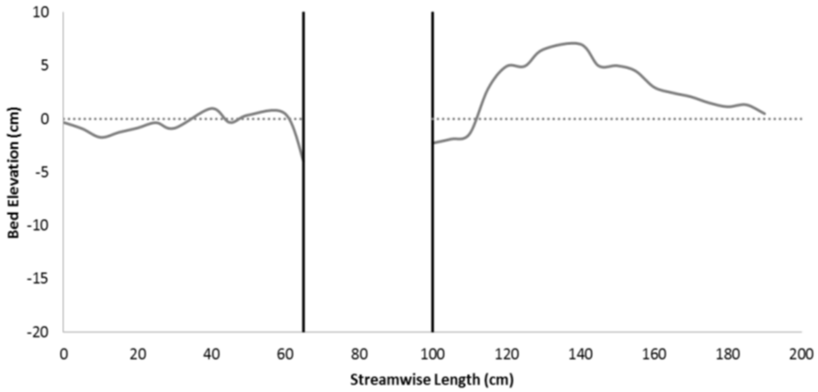

Test 10

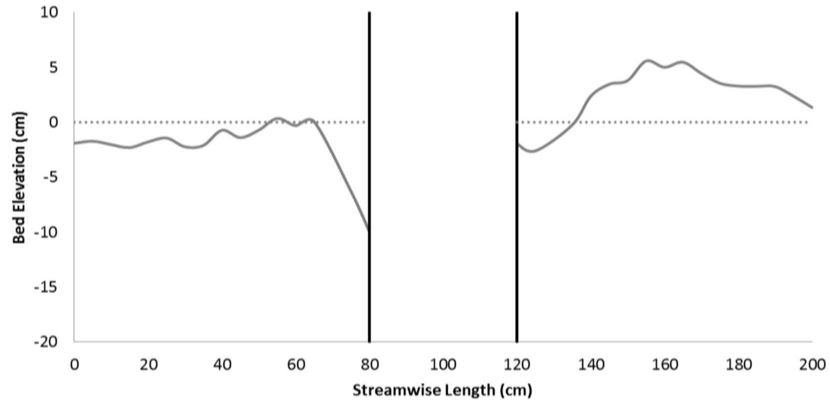

Legend